RICE UNIVERSITY

Magnetoelectric Materials for Wireless Power Delivery to Miniature Bioelectronic Implants

By

Amanda Singer

A THESIS SUBMITTED
IN PARTIAL FULFILLMENT OF THE
REQUIREMENTS FOR THE DEGREE

Doctor of Philosophy

APPROVED, THESIS COMMITTEE

Jacob Robinson (Apr 28, 2021 16:02 CDT)

Jacob Robinson
Associate Professor, Electrical and Computer Engineering and Bioengineering, Rice University

Matthew McGinley
Assistant Professor, Neuroscience, Baylor College of Medicine

Chong Xie
Associate Professor, Electrical and Computer Engineering, Rice University

Geoffrey Wehmeyer
Assistant Professor, Mechanical Engineering, Rice University

HOUSTON, TEXAS

April 2021

ABSTRACT

Magnetoelectric Materials for Wireless Power Delivery to Miniature Bioelectronic Implants

by

Amanda Singer

Advances in implanted bioelectronic technology offers the opportunity to develop more effective tools for personalized electronic medicine. While there are numerous clinical and pre-clinical applications for these devices, power delivery to these systems can be challenging. Wireless battery-free devices offer advantages such as a smaller and lighter device footprint and reduced failures and infections by eliminating lead wires. However, with the development of wireless technologies, there are fundamental tradeoffs between five essential factors: power, miniaturization, depth, alignment tolerance, and transducer distance, while still allowing devices to work within safety limits. Here I briefly discuss five existing types of wireless power transfer technologies used in bioelectronic implants - inductive coupling, radio frequency, mid-field, ultrasound, and light -and review them in context of the five tradeoffs listed above. I then add a new alternative wireless power method based on magnetoelectric (ME) materials which combines the advantages of ultrasound and inductive coupling (miniature devices activated from a distance away) to deliver therapeutic stimulation in excess of 100 Hz. I demonstrate that wireless ME stimulators provide deep brain stimulation in a freely moving rodent model for Parkinson's disease and that these devices can be

miniaturized to mm-scale and fully implanted. These results suggest ME materials are an excellent candidate to add to the fundamental types of wireless power techniques and enable miniature bioelectronics for clinical and research applications is situations where other types of wireless power transfer may be limited.

Acknowledgments

There are so many many people to thank for making this work possible. I have such respect for Rice University and especially the environment within the applied physics and electrical engineering department for creating an encouraging culture of successful research and a supportive community to work in. Special thanks to my advisor Jacob Robinson for his support and mentorship over the years. Thanks also to all the members of the Robinson Lab for being great people to work alongside and learn from. Also many thanks to Caleb Kemere and Shayok Dutta, Eric Lewis, and Ziying Chen for making the in vivo results in this work possible.

Outside of Rice, thanks to my sisters for only being a phone call away and always willing to share crazy stories (at least our version of crazy). Thanks to my parents for their support. Special thanks to my new Singer family for welcoming me with open arms and always being willing to help with the little things that make a PhD possible, from dog sitting to occasionally being my convenient mailing address.

Finally, and most importantly, thanks to my husband Nathan. Part of me still thinks you were a little bit crazy to want to date and marry a grad student. You've been there through quite a few of the ups and downs-thanks for always believing in me. And thanks for all the random times we had to stop by the lab for something that almost always took longer than I expected it to.

Contents

List of Figures

List of Tables

List of Equations

Chapter 1

Introduction: Bioelectronics as Medicine

1.1. A brief history of electrical stimulation

Using electrical signals to manipulate the body predates the invention of electricity, back to times when ancient cultures used electric fish for applications such as pain relief.[1] These methods became more refined with the invention of electricity, leading to various electrotherapy treatments in the 1700-1800s.[2] While the overall effectiveness of these early methods may be questionable, they highlight the important idea that electrical signals can be used for therapeutic benefit. Today, this old idea is refined and used in implantable devices such as pacemakers and deep brain stimulators (Figure 1). (Other devices such as cochlear implants, spinal cord stimulators, and foot drop stimulators are also common implants that operate similarly.) In these devices an implanted pulse generator delivers a specific electrical signal to an electrode placed in the target area. Currently these types of

implants are a last resort for very specific applications when other types of pharmaceuticals are not effective. However, due to recent addictive pharmaceutical issues such as the “opioid crisis”, researchers are once again looking at electrical implants as a non-addictive alternative to broader applications including chronic pain.[3] There is a need for new classes of “bioelectronics” to meet a growing demand as we continue to equate electronics with medicine.

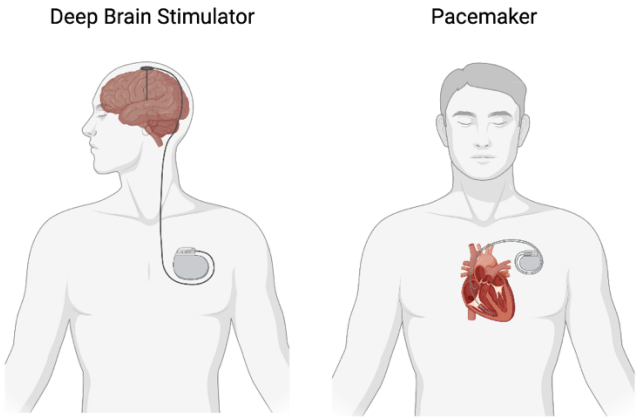

Figure 1 Examples of electrical stimulators in use today-deep brain stimulator and pacemaker

Chapter 2

Wireless Power Delivery to Bioelectronics

2.1. Wireless power delivery techniques fulfill a critical need in bioelectronic implants

As mentioned previously, advances in bioelectronic medicine are continually driven by new developments in targeted electronic devices that stimulate and sense physiological processes in the body. In humans we see examples of these technologies in devices such as pacemakers, brain electrodes, glucose monitors, cochlear implants, and spinal cord stimulators. Recent progress in materials and fabrication resulted in new devices that are softer and more flexible and electrodes that have lower impedance[4–6]. This variety of tools allows researchers and clinicians to tailor bioelectronics for specific applications in humans and animal models. Similarly, we believe there are similar opportunities for materials advances to improve the way we deliver power to these bioelectronic devices.

Wireless, battery-free technologies offer a number of advantages for both preclinical testing and clinical applications. Most bioelectronic implants currently used in a clinical setting are battery powered, often with leads extending from an implanted pattern generator (IPG) to the stimulation target. While battery power ensures that these devices are reliably powered, it also adds surgical complexity due to the larger device size and introduces potential issues with lead migration and disconnection over time[7–9]. It also limits the placement of devices to areas where leads can be placed between the battery and the target tissue, or, in the case of leadless batteries, to surgically accessible areas where the device will fit[10,11]. Wireless, battery-free devices are generally smaller and can be placed in specific, previously inaccessible, locations without lead wires. Furthermore, in preclinical work in animal models, especially rodent models, there is a need to interface with even smaller target areas which are impractical to target with large battery powered devices. In some cases, tethered devices, where an external supply powers an implanted device, are sufficient, however these tethers can interfere with natural behavior and are challenging to use for chronic studies[12]. Miniature wireless devices offer advantages of accessing small target areas in ways that allow for unimpeded motion (Figure 2**,** References[13–18]).

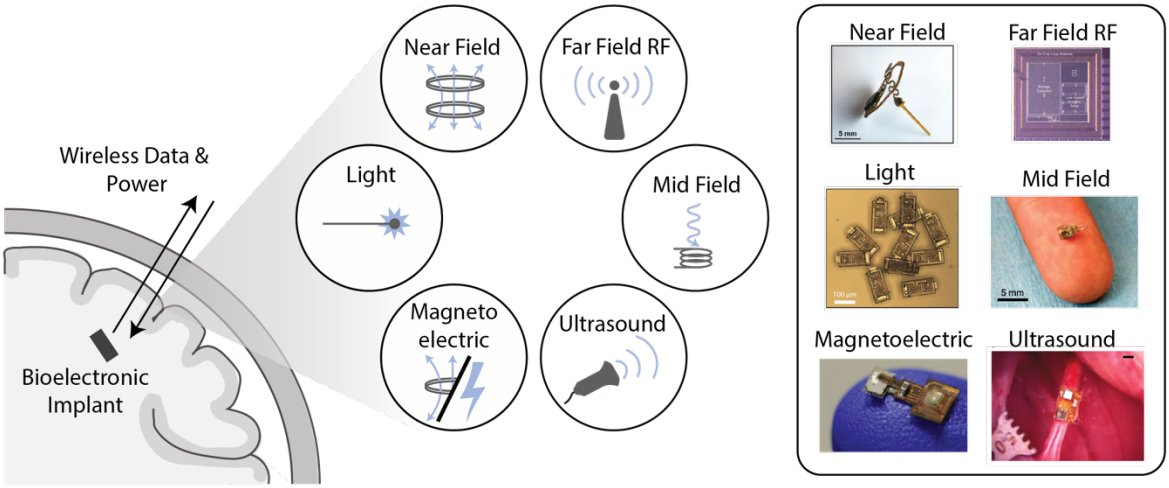

Figure 2 Different power modalities for wireless bioelectronic implants

Technology challenges for wireless power delivery often depend on whether one is working with a small model, large animal, or human, and where in the body the implant is located. For example, the geometry of the nervous system varies dramatically across humans and animal models (Figure 3**,** References a[19,20], b[21], c[22], d[23], e[24], f[25]). A rodent brain is only 1-2 cm long, while a human brain is 10-15 cm[26]. Similarly, a rodent vagus nerve is significantly smaller than in a human or larger animal model vagus nerve[27]. In a simple sense, this means that technology designed for larger animals may not need to be miniaturized to the same degree as a device designed for a mouse; however, the wireless power may need to propagate through a significantly greater distance in bone and tissue. On the other hand, bioelectronics designed for rodent models must be small and lightweight but need not operate at the same depths within the tissue. Furthermore, the electrical current levels required to stimulate various nerves electrically also differ depending on the animal and target application (Figure 3).[18,20,22–25] This naturally existing intricacy in biological systems adds extra layers of complexity to developing wireless bioelectronic devices. As a result, optimal wireless power transfer technologies clearly change depending on the animal model or clinical target.

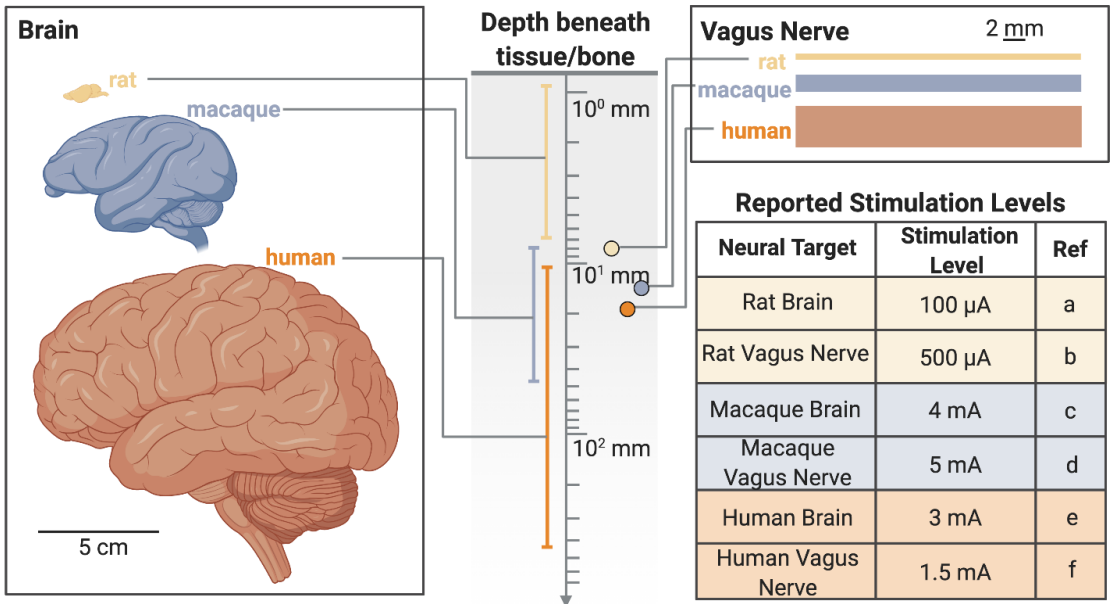

Reported Stimulation Levels

Neural Target	Stimulation Level	Ref
Rat Brain	100 µA	a
Rat Vagus Nerve	500 µA	b
Macaque Brain	4 mA	c
Macaque Vagus Nerve	5 mA	d
Human Brain	3 mA	e
Human Vagus Nerve	1.5 mA	f

Figure 3 Size and depth differences in anatomical targets lead to a need for a variety of wireless power schemes for implanted bioelectronics.

Safety limits and crossing between different media like air and bone add to the challenges facing wireless data and power transfer to implanted bioelectronic devices.[28] Wireless links between a transmitter and receiver are significantly less efficient than a direct wired connection and much of the transmitted power is lost along the path between the implant and transmitter. This can be due to the geometry of the system as well as reflected power due to impedance mismatches at the boundaries of air and different types of tissue. In order to account for this and deliver a suitable amount of power to the implant, systems will increase the amount of power applied by the transmitter. However, in doing this the human body cannot be exposed to excessive amounts of heat or electromagnetic radiation. These safety requirements restrict the applied power levels and thus help to set the maximum power available to the implant. Many types of implants can also require an onboard charge storage capacitor to deliver sufficient charge to an implant which can limit the operating frequency of the device and increase the device footprint.

To overcome these challenges researchers have developed a number of wireless data and power transfer technologies for implanted bioelectronic devices, each with advantages and disadvantages when compared to alternative approaches (Figure 4, References[17–20,29–40]). Over time, devices have generally been made smaller and more efficient moving from devices that could only be used in large animals to millimeter-sized devices compatible with rodents (Figure 4).

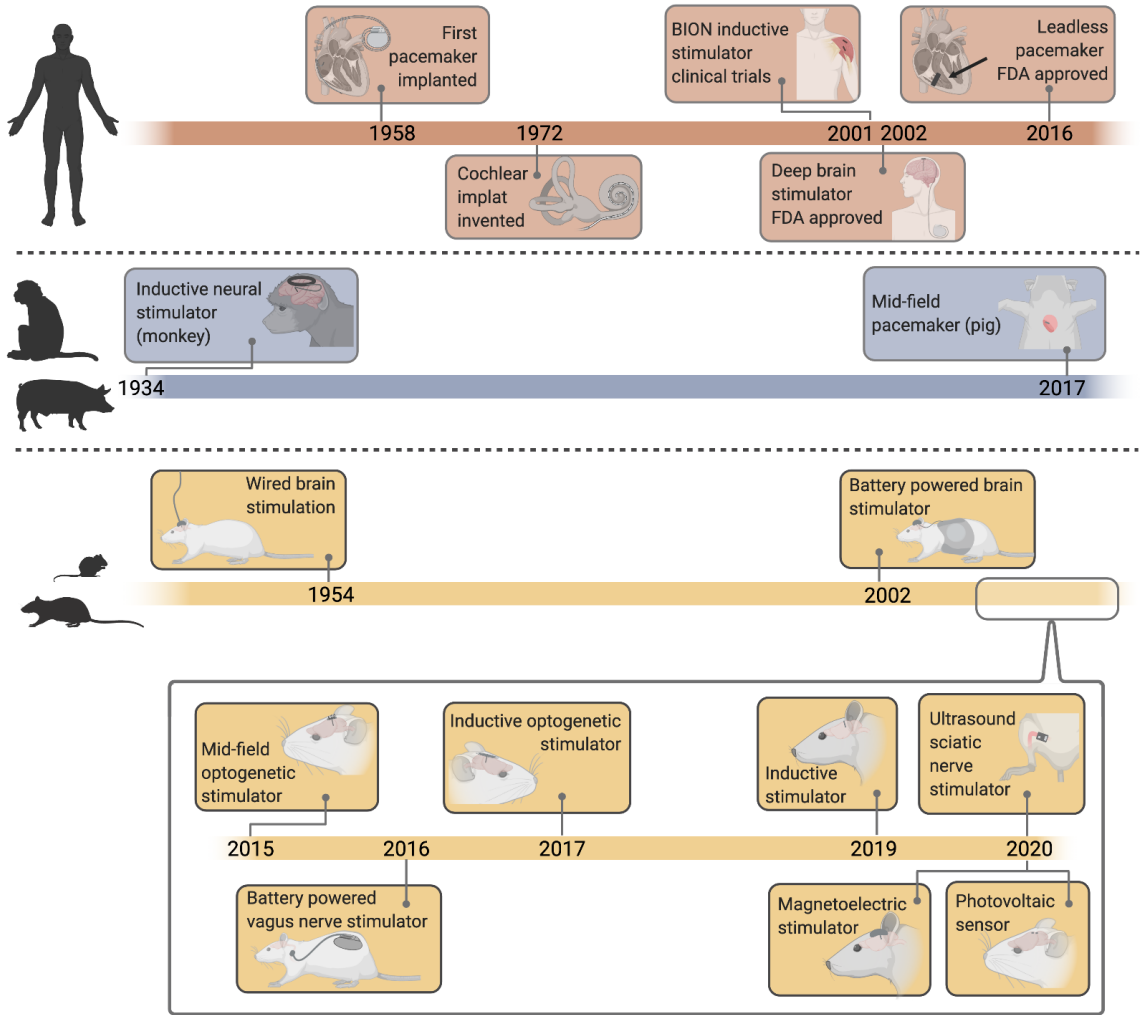

Figure 4 Timeline of bioelectronic power delivery methods in various clinical and preclinical applications shows a variety of recently proposed wireless power delivery solutions, especially in rodent models

2.2. Fundamental tradeoffs for wireless power transfer

With the expanded library of WPT technologies we sought to understand the strengths and weaknesses of each approach by comparing them based on five metrics that are typically the major design considerations for bioelectronic implants: miniaturization, depth, alignment tolerance, transducer distance, and power (Figure 5).

We define miniaturization as the longest length of the wireless power receiver on the implant (which usually correlates with the longest length of the device). Depth refers to the depth in tissue an implant can be, which is often directly related to the safety limits of the power type or the geometry of the device. Alignment tolerance is the sensitivity of the device to a combination of angular and translational misalignment. We estimated this metric by multiplying the approximate angular alignment tolerance by the approximate translational alignment tolerance. We define the angular alignment tolerance as the fraction of angles between 0 and 90 where the device receives sufficient power to function. Similarly, we define the translational alignment tolerance as the fraction of the area of a 10 cm diameter circle within which translational misalignment still results in the device receiving sufficient power to function (up to 5 cm translational displacement in any direction). Transducer distance is the distance the wireless power can reliably transfer through air, which is especially important in freely moving rodent applications. Power refers to the power the implant can generate. While these factors are all interdependent to a point (i.e., a smaller or deeper implanted device will generate less power), there are also fundamental limitations for each type of wireless power technique which allow us to estimate the design space available for each different modality. Here we focus on near field inductive

coupling, far field antenna, mid-field inductive coupling, ultrasound, and photovoltaic techniques since these technologies have been demonstrated in vivo.

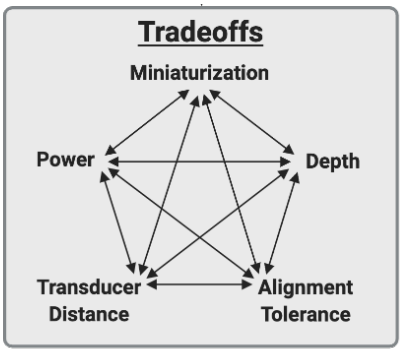

Figure 5 Five fundamental tradeoffs for wireless power delivery

To visually compare the main WPT technologies for bioelectronics we categorized the technologies based on the type of transmitter and the type of receiver and compare their performance according to the 5 metrics described above (Figure 6, References a[15], c[16,31], d[32], e[18], h[14,30], i[17]). The four basic transmitter types used to send wireless power into the body are electromagnetic antennas, ultrasound transducers, magnetic coils, and light (usually infrared). These types of transmitters couple power into an implant that contains either an antenna, acoustic material, coil, or photovoltaic component. We then plotted each of the five metrics on a separate axis with our estimation of where the fundamental limits for each factor lies based on the physics of each technique and the limits imposed by biological geometry and safety. It should be noted that the shaded boundary represents our estimated limit for each metric and not the space that any particular device would occupy. In other words, we expect any instantiation of a wireless device to fall within the shaded region. As examples, we plotted the performance of numerous devices reported in the literature on the radar plots showing that they all fall within the shaded regions.

In the following sections we explore the fundamentals of five major WPT technologies considered here and discuss other WPT methods.

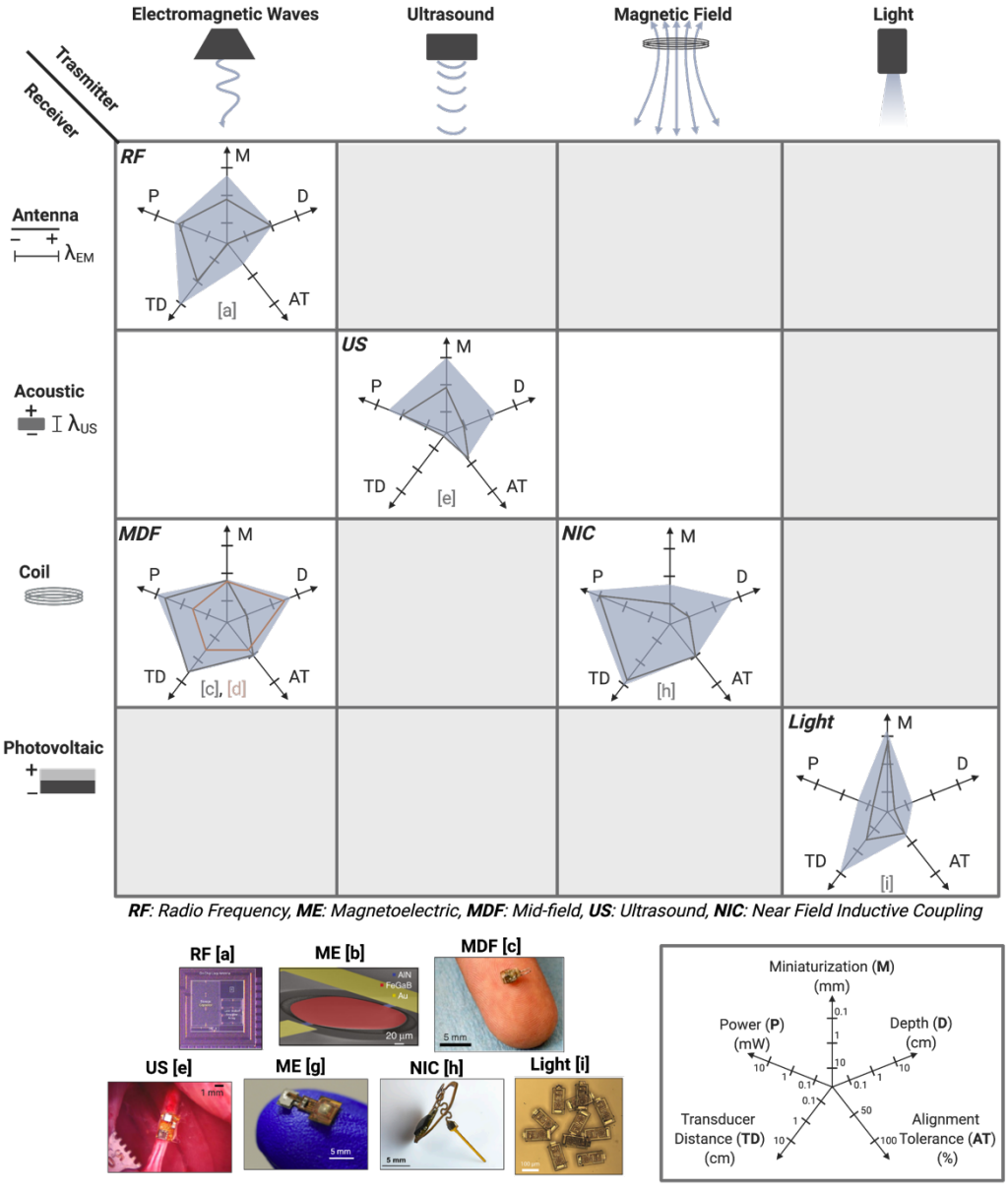

Figure 6. Comparison of wireless power delivery methods based on five metrics: Miniaturization (M), Depth (D), Alignment Tolerance (AT), Transducer Distance (TD), and Power (P) shows the possible application spaces for each of five major forms of WPT.

2.3. Wireless Power Transfer Methods

2.3.1. Near Field Inductive Coupling (NIC)

Near field inductive coupling (NIC) is one of the most commonly used methods of wireless power transfer to implanted bioelectronic devices. This method uses an external coil (or in some cases a loop antenna) to generate an alternating magnetic field that is transferred through tissue to a second, smaller, implanted coil (Figure 7, References b[30], c[41], d[35]).[14,30,35,41–43] This method of wireless power transfer is attractive due to the fact that magnetic fields at these frequencies can safely pass through tissue from a small distance away with little or no attenuation.[44] While it is often referred to as radio frequency in literature, the magnetic fields here do not radiate as radio frequency electromagnetic waves. We discuss radio frequency electromagnetic waves for far-field technologies WPT in a later section.

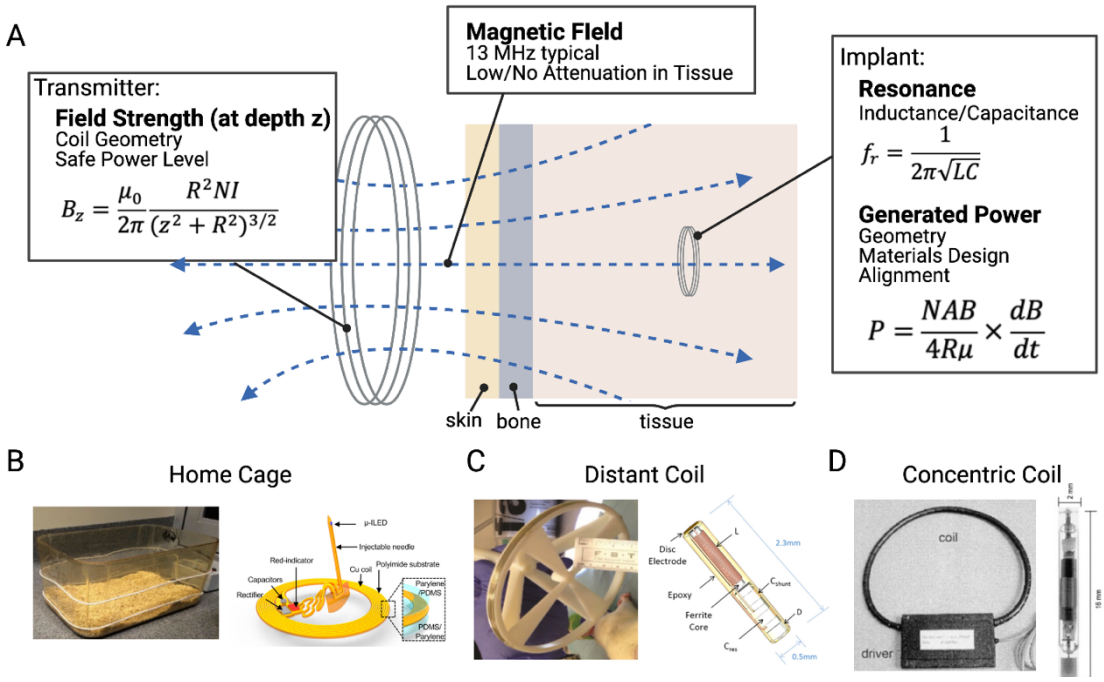

Figure 7 Near field inductive coupling A) uses a transmitting coil to power a smaller implanted coil using alternating magnetic fields. This type of system can be used in B) home cages, C) coils from a distance away, and D) coils placed around a peripheral limb.

When considering NIC for miniature bioelectronics one must consider two primary factors: 1) the strength of the magnetic field at the depth of the implant - which depends mainly on the transmitter geometry and current, and 2) how much power can be harvested from a magnetic field of a given strength - which depends on the receiver size and location.

For a circular coil transmitter, the field strength *B* at a distance *z* from the center of the coil can be written as (Equation 1):

$$B_z = \frac{\mu_0}{2\pi} \frac{R^2 NI}{(z^2 + R^2)^{3/2}}$$

Equation 1

Where *R* is the radius of the coil, *N* is the number of turns in the coil, and *I* is the current through the coil. These three factors can be tailored to optimize for a specific application. Increasing the number of turns or current in a coil will always increase the field strength but changing the radius of the transmitting coil can either increase or decrease the field strength depending on the implant depth. For example, when powered with the same current, smaller coils produce a larger magnetic field at a shallow depth than larger coils. However, because the field strength falls off more slowly as a function of depth from a large coil, large coils are more effective for powering deeper implants. While there are many opportunities to optimize the coil designs to improve performance for a given application, it is generally preferable to increase the radius of the transmitter for deeper implants rather than trying to increase the transmitter current (e.g., Freeman et al.[41] (Figure 7 C)).

In NIC the magnetic field induces a voltage and current in the receiving bioelectronic that is proportional to the magnetic flux captured by a small implanted coil. The power generated by an inductively powered implant depends on the area of the pick-up coil, the number of turns, and the strength of the magnetic field. For a circular coil geometry, the power received at the implant can be written as (Equation 2)[45]:

$$P = \frac{NAB}{4R\mu} \times \frac{dB}{dt}$$

Equation 2

Where N is the number of turns, A is the area of the implanted coil, R is the radius of the implanted coil, and μ is the permeability of the implanted coil.

Two important design considerations emerge from the received power equation as it relates to miniature bioelectronics.[46] First, A is the area perpendicular to the magnetic field, so in addition to the physical dimensions of the coil, any angular or translational misalignment will reduce the received power. Second, as a device is made smaller, the area and the number of turns must be reduced. Thus, the received power falls dramatically as a function of radius of the receiver (typically as R^3).[45] The received power can also be increased using the transmitter to increase the transverse component of the magnetic field at the implant location (B_z) or the frequency of the applied field (dB/dt).

Another important consideration is the resonant frequency, f_r, for which power transfer is maximized. For NIC this resonance is determined by the inductance of the coil (L) and the total capacitance of the receiver (C), which is typically tuned by changing the value of the capacitor in the circuit (Equation 3):

$$f_r = \frac{1}{2\pi\sqrt{LC}}$$

Equation 3

In many cases, inductively powered systems are designed to resonate at 13 MHz. There are three main reasons for this. First, this is a commonly used frequency band and is therefore a practical choice due to the fact that many off-the-shelf components are already designed to work in this range. Second, there is a balance between increasing the frequency to increase the power of the implant (Equation 2) and electromagnetic safety limits which reduce the amount of power that can be

safely applied by the transmitter at higher frequencies due to tissue absorption and the range between 1-13 MHz is generally a considered good choice for safe but effective WPT for bioelectronics. And finally, even though the power will increase with increasing frequency, some implants also use a ferromagnetic core to increase the captured flux, and these cores become lossy at frequencies higher than this.[41] In some cases, these types of implants will even operate at lower frequencies to account for this such as the BION system which operates at 2 MHz and the system used by Maeng et al. which operates at 10 MHz.[29,35]

So, while in theory a high magnetic field strength at a high frequency applied to a large well-aligned implanted resonant coil will generate a large amount of power, we see that this is not always safe or practical. When we move away from this idealized picture to more realistic conditions, we can evaluate this type of wireless power transfer in context of the five tradeoffs introduced previously.

Taking these considerations into account we can plot the expected performance envelope for NIC bioelectronics (Figure 6) according to the five performance metrics described in Figure 4. Because the power falls considerably as the devices are miniaturized, NIC performs best for relatively larger devices in the range of 5-10 mm in diameter. At these sizes, inductively powered implants can achieve upwards of 10 mW of power within safe magnetic field conditions.[30] In certain geometries, especially in cases where the coils that power the implant can be wrapped around the implant locations (e.g., peripheral limbs or rodent home cages Figure 7 B,D), this technique can achieve good depth and transducer distance, up to approximately 10 cm.[30,35] These factors are limited by the maximum field strength the transmitter can safely transmit at typical inductive frequencies and the spatial decrease in field strength. Furthermore, because these implants directly depend on the magnetic flux through the coils, especially for the case of an air core coil, the alignment tolerance reduces to approximately 50%. This means that while NIC implants can operate

with some misalignment, they are more suited for applications where alignment is not expected to exceed more than roughly 30 degrees for extended periods of time, such as cochlear implants where the two coils are fixed and aligned with each other.

One approach to improve the alignment tolerance is to overpower the implant so that it will still be sufficiently powered even in a lower field strength from misalignment such as in rodent home cage applications.[30] For example, Shin et al. demonstrated a NIC system for optogenetics in freely moving mice (Figure 7 B). In this case a shallow (0.1 mm) lower power (10 mW) implant in a mouse was powered from up to 10 cm away from loop antennas wrapped around a cage. In another case, Maeng et al. used a more miniature inductive coil (which used a ferromagnetic core) with a length of 2.3 mm implanted 7.8 mm deep in a rat brain. In this case the implant was only able to achieve a maximum power of 0.03 mW and was powered only in one corner of a behavioral area (max transmitter distance of 10 cm).[29,41] In order to counteract the poor alignment tolerance of this device in a freely moving rat (50%), they used a combination of three coils and generated a magnetic field in three directions. The BION device is similar to this miniature elongated coil, but due to its larger dimensions and the fact that it is designed to be operated within a coil instead of a distance away, it has slightly improved power (5 mW) and incorporates charge storage components to stimulate at higher power levels.[35] This overpowering solution produces an effective solution to improve alignment tolerance at the expense of average power coupling efficiency and may push some applications close to the safety limits for magnetic field intensity. **Overall NIC performs best for relatively larger devices that require high power and do not require large angular misalignment tolerance.**

2.3.2. Far Field Antenna (RF)

Another traditional method of wireless power for bioelectronic implants uses far-field electromagnetic waves from an external antenna to transmit power to a miniature implanted receiving antenna (Figure 8, References b[15], b[47], d[48]).

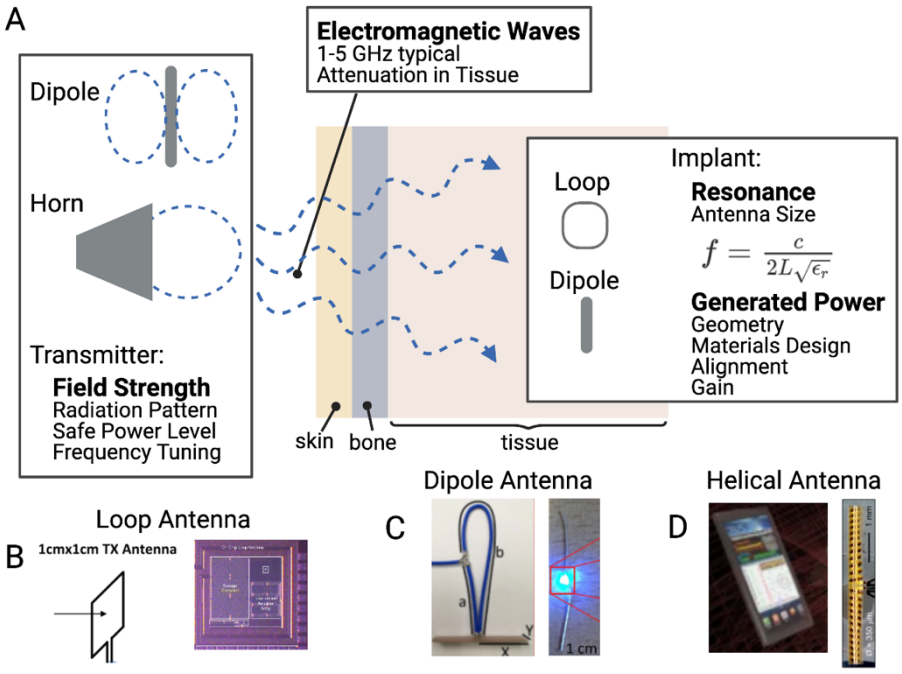

Figure 8 Far field wireless power delivery systems use a transmitting antenna to power an implanted antenna using radiating electromagnetic waves (A). Multiple types of implanted antenna systems have been suggested including B) loop antennas, C) dipole antennas, and D) helical antennas.

While near-field pickup coils discussed in the previous section can also be classified as loop antennas, there are fundamental differences that separate antennas from near-field pickup coils as we define them here. A loop antenna operating at low MHz frequencies can almost always be classified as an inductive coil due to the fact that every coil and relevant distance is considerably smaller than the electromagnetic

wavelength at these frequencies (~10-30 m) and thus they operate using the near field magnetic field to power implants. However, as the frequency increases to the GHz range, transmitting antennas (including loop antennas) can be designed with features that are on the scale of a wavelength or fraction of a wavelength. For example, at 2.4 GHz and 5 GHz (common frequency bands) the electromagnetic wavelength is only about 12 cm and 6 cm respectively. Quarter and half wavelength antennas, though less efficient, are also common. At these higher frequencies, once a device is a few cm away from the transmitter, this is considered the "far-field" where the electric and magnetic components combine into a radiating electromagnetic wave. In this regime the power transfer is unlike NIC where the electric and magnetic components were separate and localized. Aside from loop antennas, some other simple types of antennas found in bioelectronic applications include horn antennas and dipole antennas.[47–52]

On the implant side, while loop antennas are primarily powered by the magnetic component of the EM wave, dipole antennas are activated by the electrical component as the standing wave condition is reversed and transformed into electrical power fed to the implant from the center of the antenna. In each case the resonant condition for both the transmitter and receiver is set by the length of the antenna trace. For a half wave dipole antenna this can be written mathematically as:

$$f_r = \frac{c}{2L\sqrt{\varepsilon_r}}$$

Equation 4

Where L is the length of the dipole and ε_r is the relative permittivity of the tissue. Aldaoud et al. demonstrated using this type of device to wirelessly light implantable LEDs (Figure 8 C).[47] Other antenna types such as loop (Figure 8B) and helical

(Figure 8D) antennas can also be designed with trace lengths tuned to a specific frequency, making far field antenna one of the most geometrically versatile classes of wireless power.[15,48,53]

In many cases the types of antenna chosen for the transmitter and receiver depend on multiple factors for each antenna which can include gain, power transfer efficiency, and the radiation pattern. Antenna gain is a commonly reported value and generally refers to a comparison of the measured transmitted or received power of an antenna with an "ideal" antenna. It is measured in units of decibels, dBi or dBd depending on whether the comparison is to an "isotropic" or "dipole" ideal antenna. A higher gain indicates that an antenna can transmit or receive a higher amount of radiated power in a certain direction. Power transfer efficiency is simply the ratio of the power captured by the implant to the power input to the transmitter. Typical values are usually less than 1%.[45] These efficiency values are important for antenna power transfer (and also for NIC) because these methods are usually operating near the safety exposure limits, so higher efficiencies are needed to increase the received power at the implant. The radiation pattern is also an important consideration for both the transmitter and receiver as it helps to determine alignment tolerance. Radiation patterns are plots of the gain in the various directions an antenna can radiate and absorb EM waves. For example, as mentioned earlier, horn antennas are highly directional, while dipole antennas are omnidirectional and will therefore have very different radiation patterns (Figure 8).

Implants that use EM power transmission, while not the best choice for transmitting high levels of power, are particularly useful for data transmission to and from an implant. For example, Bluetooth transfer systems use a form of RF data transfer.[54–56] Systems that use RF power for freely moving rodent experiments also may need to implement a tracking system to efficiently deliver power without exceeding safety limits.[53]

Propagating EM waves can be advantageous, especially in applications where minimizing losses through distance in air is important. If we look at the practical application space for far field antennas (Figure 6) we first note that the received power is generally low with a maximum around 1 mW due to the low power transfer efficiency. These types of implants can be miniaturized but again with a corresponding drop in efficiency as the fractional wavelength gets smaller. In practical terms, depending on the application, just under one mm is the size devices can shrink to and still receive enough power to power an implant. The depth in tissue an antenna can be implanted is relatively shallow (up to ~ 1 cm) due to the safety limits and absorption of EM waves in tissue. Because EM waves at these frequencies can travel long distances in air, the transmitter distance can theoretically be quite large, even if the transferred power is low.[57,58] As suggested by the radiation patterns, the alignment tolerance depends on the type of antenna used for transmitting and receiving but is generally low (here we suggest approximately 25%). For example, Rahmani et al. developed a 2.56 mm^2 loop antenna implant that can be powered by a transmitting loop antenna several cm away capable of generating 1.2 mW of power.[15] **Overall RF devices are best suited for cm-sized devices implanted at shallow depths below the skin where it is important to achieve reliable long-range data communication.**

2.3.3. Mid Field Inductive (MDF)

A special case of wireless power delivery which combines different aspects of inductive and far-field methods, mid-field powering (Figure 9, References b[31,32],c[32]), was demonstrated in mice and pigs by Montgomery et al and Agrawal et al, respectively.[31,32,59] Traditionally the term “mid-field” applies to a geometric region in the transition area between near field and far field. However, the methods

described here and the physics behind the design deviate somewhat from this standard view.[16,31,32,59–62]

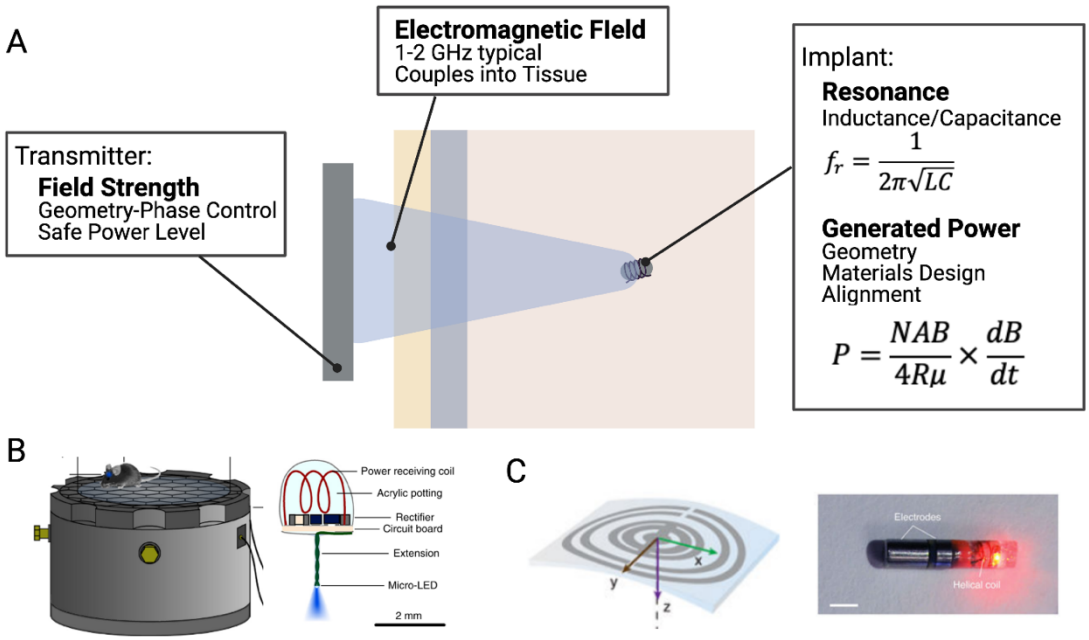

Figure 9 Mid-field wireless power transfer uses an antenna type transmitter to deliver power to an inductively powered stimulator. This method has shown efficacy in B) freely moving mice and C) large animal models

In this method a custom designed antenna delivers power to an implanted miniature inductive coil. Though the geometry is smaller, the implant design is fundamentally similar to those discussed in NIC with a small coil of wire attached to a capacitor to determine a resonant frequency.

The transmitters, on the other hand, while relying on some of the principles discussed in RF antennas, are more customized to biological tissue. Rather than solely considering the resonances and wavelengths associated with the antenna

hardware design, mid-field powering focuses on how those properties change in tissue due to the change in the dielectric properties.[45,63] Indeed the "mid-field" nomenclature partially refers to the fact that 1-2 GHz electromagnetic wavelengths, without considering fractional wavelengths, are shorter in tissue (2-3 cm) than in air (15-30 cm), meaning that if we consider most of the field to be in tissue (as is the case with deeper implants), we are operating at the transition area between near and far field. This allows this method to make use of both the near field and radiating field effects.

More importantly, mid-field powering makes use of the fact that fields at these frequencies are strongly absorbed by tissue. Normally, this would be avoided for safety concerns, but manipulated properly this means that the tissue can help to transmit, focus, and amplify the original EM waves, allowing for deeper penetration to small implants.

Various mid-field transmitters have been designed for different applications, however in general, they all follow the same basic principle. A resonant antenna (or cavity) transmits an electromagnetic signal a specific predetermined frequency, which, based on the antenna transmitter design, does not propagate well in air and thus only near field components can be observed. However, when the near field is in close contact with tissue the field will radiate into the tissue layers as a propagating EM wave due the change in dielectric properties. This radiating wave can also be focused by further designing the transmitting antenna. The EM wave propagates through tissue and the losses that come not with geometric fall off as in the case of near field, but with losses from absorption of the electric field in tissue. An implant several cm deep in tissue can then be inductively powered by the magnetic component of the EM wave. The power the implant can generate is mostly limited by the amount of incident power that can safely be applied by the transmitter.

In practice these transmitters can range from simple to complex depending on the application. For example, in the case of an experiment in a freely moving mouse, simply tuning the wavelength of the near field applied by a resonant cavity to 1.5 GHz (which is shown to be resonant with a mouse tissue model) was enough to power miniature electrical and optical implants.[31,59] In the cases of implants that were deeper in tissue, different tissue layers and field focusing had to be taken into account, which necessitated a more complex transmitter design where phase delays between different ports were used to cause appropriate interference of the original EM waves.[32] The optimal EM frequency used also depends on the target application as the dielectric properties can be different for different tissue layers and thicknesses in different areas of the body.[52,63]

In context of the five tradeoffs, mid-field wireless power systems show good all-around performance (Figure 6). Depending on the specific setup, power levels can typically reach a few mW with up to 10 mW for shallower configurations. The size can reduce down to about 1 mm with implantation depths up several cm through skin bone and tissue. The transducer can be placed a few cm away and does not need to be in direct contact with the tissue. Because this is similar to an inductive effect, the alignment tolerance is similar to an inductive system (50%). An added advantage of this technique compared to other recent novel methods at this point in time is its demonstrated versatility in multiple applications across model animals. For example, in freely moving mice (Figure 9 B) the depth in tissue was less important, allowing for the other four factors to be more optimized. In a separate case, Agrawal et al. used this method to demonstrate heart pacing in a porcine model. Here, the depth is more important while the transmitter can be placed closer to the skin in a fixed position. The major challenge for human translation is that typically operating powers require transmitted power that is close to the approved safety limits.[32] **Overall, mid-field power transfer is a good choice for mm-sized devices, but because these devices operate near the safety limits using**

absorbed EM radiation they are typically best for shallow implants or for deep implants that require less than 1 mW average power.

2.3.4. Ultrasound (US)

Recently, ultrasound has emerged as a popular choice for powering mm-sized bioelectric implants that use piezoelectric receivers to harness acoustic energy (Figure 10, Reference b[18]).[18,64–67] Unlike the previous methods, which used electric and magnetic fields to transfer power, ultrasound uses high frequency sound waves. These waves transmit well through certain types of tissue and are traditionally used for biological imaging but have recently gained popularity as a way to transfer power to miniature implants, such as "neural dust" and "Stim Dust."[18,64]

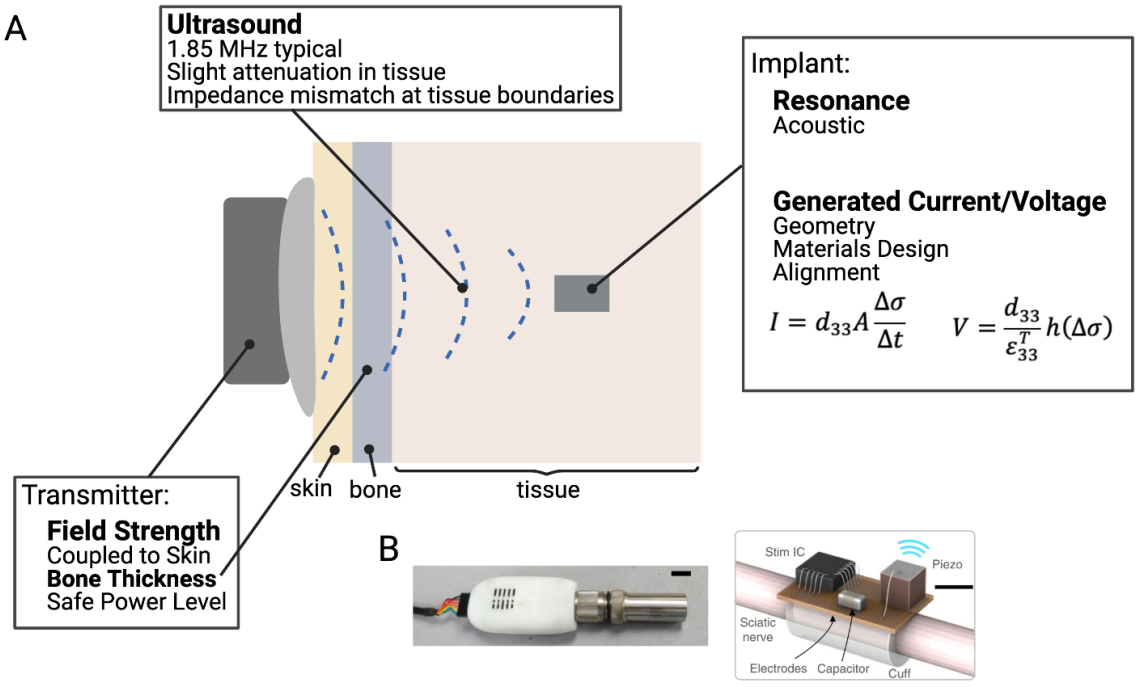

Figure 10 Ultrasound wireless power transfer uses an ultrasound traducer in contact with the skin to deliver power to miniature implants, such as those developed by Piech et al. (B).

While ultrasound excels at delivering power deep in tissue, one drawback is that ultrasound is highly sensitive to impedance mismatches between different types of materials. For example, if the materials have different acoustic properties the ultrasound wave will primarily reflect back instead of being transmitted across the boundary. For bioelectronic applications acoustic reflections often occur at the boundary between air and tissue and, to a lesser extent, boundaries between tissue and bone. Practically, this means the ultrasound transmitter must be placed in direct contact with the skin, acoustically coupled by placing a gel between the transducer and skin. It also cannot operate in the areas of the body around the lungs.[68,69] In areas completely encased in bone, such as the brain, transmission can be complicated and will require specially designed focused ultrasound transmitters.[70,71] In more simple peripheral nerve applications researchers can usually use traditional readily available ultrasound transmitters.

Ultrasound powered implants usually contain a piezoelectric element which transduces the ultrasound energy to electrical energy through a vibrating resonant mode. The piezoelectric materials develop a voltage across them in response to the applied stress by the incident ultrasound waves. For example, unstressed lead zirconate titanate (PZT), a commonly used piezoelectric material, has a cubic crystal form with Ti or Zr at a neutral point in the center of the cube. However, under mechanical force, the crystal shape changes and displaces the central Ti or Zr and the crystal develops an electrical polarization and generates electrical energy.[72] In general, the voltage a piezoelectric material generates can be written as (Equation 5):[73]

$$V = \frac{d_{33}}{\varepsilon_{33}^{T}} h(\Delta\sigma)$$

Equation 5

From this expression the relevant factors to determine the voltage a piezoelectric material will generate are the thickness h, the applied stress $\Delta\sigma$, and two material constants d_{33} and ε_{33}^{T}. d_{33} is a piezoelectric coefficient and ε_{33}^{T} is the permittivity (which is related to the capacitance of the material). The subscripts for these two constants depend on the directional relationship between the polarization and the applied stress. The most common modes are d_{31}/ε_{31} (for polarization across the thickness and stress applied along the length) and d_{33}/ε_{33} (for polarization and stress applied across the thickness). Other modes are also possible, but less likely to be used in biological applications. One thing to note about the voltage is that the only geometric dependence is on the thickness of the piezoelectric material, which gives an advantage for miniature devices compared to an implanted coil where the voltage depended on the area.

An expression for the current from a piezoelectric can also be written (Equation 6):[73]

$$I = d_{33} A \frac{\Delta\sigma}{\Delta t}$$

Equation 6

As expected for a capacitive material, here we see a dependence on the area (A) of the material. Another thing to note for implant design is that both of these expressions highly depend on the piezoelectric coefficient. Indeed, the reason PZT is so commonly used is due to its coefficient of 100-500 pC/N, which is relatively large compared to other materials.[74]

Similar to other types of implants, the available power an implant can generate can be increased under resonant conditions, which exist for the different modes described earlier. The resonances used in piezoelectric implants are similar in fundamentals to those used in far field antennas, where the size of the device is on the order of a wavelength. However, in this case we must consider the acoustic wavelength which is 10^5 times smaller than the EM wavelength for a given frequency. This means that resonant piezoelectric devices can be made much smaller and more efficient than an EM antenna at the same frequency. The safety standards are also different (and higher) for ultrasound waves since they are not absorbed by the body as easily as EM waves.[28,75]

Any bioelectronic implementation using ultrasound as the wireless power method can potentially suffer from the tradeoff of having to put the transmitter in contact with the skin (zero transducer distance) (Figure 6). However, it has advantages in miniaturization over more traditional methods due to the acoustic resonance with the potential for future sub-mm size devices. The other tradeoffs of power (several mW), depth (up to ~1-2 cm), and alignment tolerance (~50%) are moderate and within the bounds of most bioelectronic applications. For example, a "Stim Dust" implant was used to stimulate the sciatic nerve of a rodent model in a proof-of-principle demonstration.[18] Because the transmitter is already approved for imaging applications, ultrasound may be advantageous for use in peripheral targets in humans where bone and air boundaries are less of an issue. Because the coupling to ultrasound-powered devices is very sensitive to alignment errors of a few millimeters and the transmitters require ultrasound gels or foams, these devices may be best for applications that do not need continuous power like diagnostics and monitoring. **Overall, ultrasound is a good choice for mm-sized devices implanted several centimeters below the skin where there is no need for long-term continuous power or powering through bone.**

2.3.5. Light

Light is another method to deliver wireless power, and although it uses EM waves, the receiver physics and extremely short wavelengths gives it unique advantages compared to RF power. In particular, power harvesting by the receiver is typically achieved not by an antenna, but by a photovoltaic component that absorbs light within a specific wavelength range (Figure 11**,** Reference b[17]).

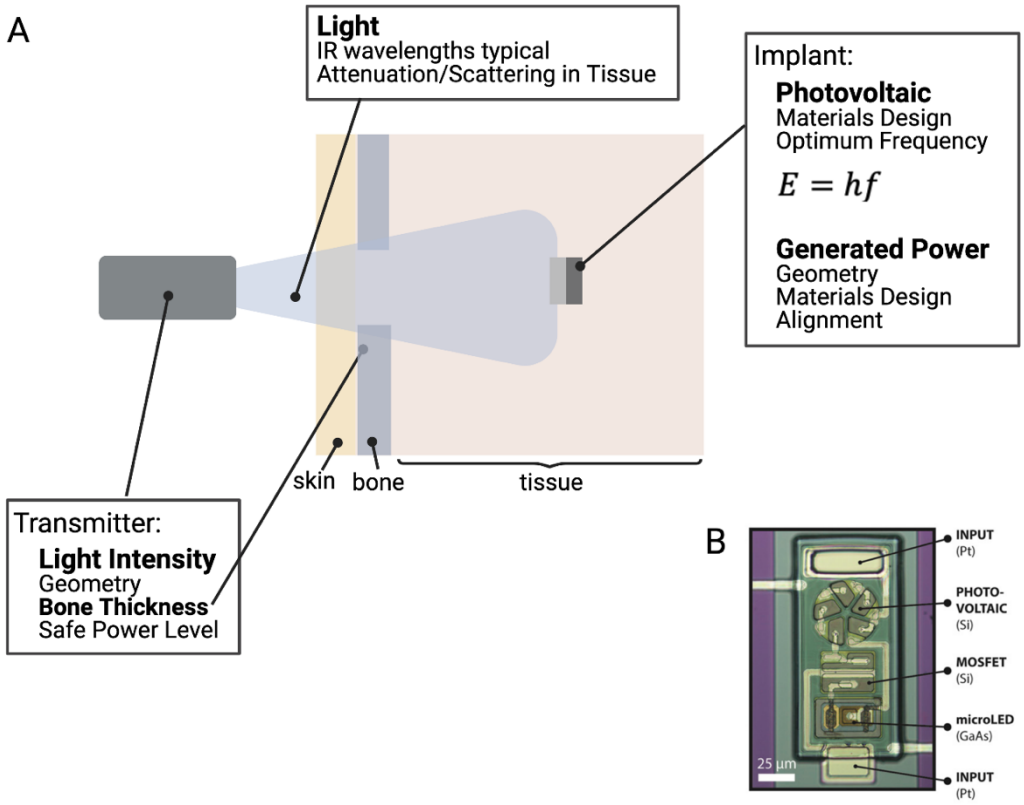

Figure 11 Wireless power transfer to implanted photovoltaics using light. While transmission through bone can be a challenge, this technique can be used to power miniature implants (B).

Light can be in the form of sunlight (which contains many frequencies of light) or from a source with a narrow frequency band such as a laser or LED.[17,55,76,77] The photovoltaic receiver is most commonly made from silicon, which means that the ideal frequency of light is about 2.7×10^5 GHz (1100 nm) which is in the near infrared range. This is determined based on the fact that the incident photons must have energy to knock electrons free within the material. This minimum amount of energy is the band gap energy and in silicon it is 1.78×10^{-19} J. The energy of a photon, which determines the optimum frequency is calculated using Planck's law (Equation 7):

$$E=hf$$

Equation 7

Where E is the energy, h is Planck's constant, and f is the frequency of the light. In theory any frequency with energy greater than the band gap energy will free electrons (ie, higher frequencies/shorter wavelengths), but in practice if the energy is too high, the electrons are knocked completely free of the material and are no longer useful. These near infrared frequencies are advantageous to bioelectronic applications because they can penetrate through tissue better than other frequencies of visible light.

These free electrons in the silicon are used to form a voltage across the thickness of the silicon which can drive implanted circuits. For this to happen the silicon must be doped with another material so charge can build up. There are two types of doping n-type and p-type. N-type doping gives the silicon an excess of negatively charged electrons and p-type gives an excess of positively charged holes (or lack of electrons). When these two materials are placed in contact with each other a p-n junction is created with a "depletion zone" in the p-type material near the boundary. In this area the excess electrons from the n-type material pair with the holes in the

p-type material. This electron-hole pair is what is knocked free by incoming photons. When this happens the electron and hole separate and travel to opposite sides of the material where the electrons can flow through the wires attached between the top and bottom of the silicon.

A major advantage of photovoltaic power generation is that because the wavelength of light is on the order of 1 um, these types of devices can be miniaturized to sub mm areas. The drawback of this extreme miniaturization is the fact that the power scales linearly with the area of the depletion region (Figure 6). The depth at which one can use light for power delivery is primarily limited by the scattering and absorption by the biological environment, which can vary depending on the thickness, type of tissue and presence of bone. In theory, because these devices could be powered by a laser, the transmitter distance can theoretically be tens of centimeters, however the distance below the skin is typically limited to a few mm due to optical scattering. For example, Cortese et al., used this wireless power technology to power miniature temperature sensors in a mouse brain (Figure 11B).[43,78] **Overall, light is often the best choice for low-power, sub-mm-sized implants at depths of several mm below the skin.**

2.3.6. Other Techniques

In addition to the major WPT technologies that have been reduced to practice, there are several emerging methods that have been proposed but have yet to be demonstrated and well-characterized in vivo.

Capacitive coupling

Capacitive coupling relies on two planar electrodes on an implant and two planar electrodes outside the body in either a monopolar or bipolar configuration.[43,78]

When a current is applied to the electrodes outside the body it acts as one side of a parallel plate capacitor, with the second side being the implanted electrode. Thus, the power travels wirelessly through the body between the two plates. The other internal and external plates are required to complete the circuit. This method generally requires a short distance between the transmitter and receiver and can require large electric fields between the plates which can interact with tissue and lead to hazardous exposure. Thus, capacitive coupling appears best positioned for low power applications, especially when angular misalignment would prevent the use of other techniques.

Self-powered devices:

Various other techniques have been proposed that differ from the traditional wireless transmitter-receiver design by converting some form of energy naturally generated in the body to electrical energy instead of using an external transmitter. One of the simplest forms of this type of device are piezo mechanical devices.[79–81] In this case an implanted piezoelectric generates energy when the body moves rather than relying on incoming ultrasound or magnetic fields to activate it. Other types of devices use electrical or chemical gradients in the body to generate power.[56,82,83]

These types of devices can be less consistent because there is no way to externally control the amount of power they will generate, and it will be difficult to operate under any sort of resonant condition. The power will therefore be fixed based on the biological environment. This may make these types of devices unsuitable for some applications such as heart pacing, where the timing is crucial. However, as implant circuitry and charge storage methods become more developed, these types of implants will be able to expand their application space.

Chapter 3

Magnetoelectrics for Wireless Power Transfer

3.1. Introducing Magnetoelectrics

The five main types of wireless power transfer discussed in the previous chapter, while sufficient for many applications highlight a space for a new class of wireless power transfer to implanted bioelectronics: magnetoelectrics. This "hybrid" wireless power uses the magnetoelectric effect to transfer power to small bioelectronic implants. This method combines some of the miniaturization advantages of ultrasound with the tissue penetration advantages of magnetic fields. Specifically using a magnetic field delivered by a near field coil or a far field antenna it is possible to activate an implanted magnetoelectric material, usually in the form of a thin bilayer film that converts an alternating magnetic field into an alternating electric field (Figure 12). Typically this conversion is made by a bilayer film where one layer contains a magnetostrictive material (which generates stress in an alternating magnetic field) and the other layer is a piezoelectric material that

converts stress into a voltage. Thus, in the presence of a magnetic field, this device will generate stress in the magnetostrictive layer which transfers to the piezoelectric layer and the resulting voltage can power to an implant similar to an ultrasonically powered piezoelectric crystal described in the previous chapter.

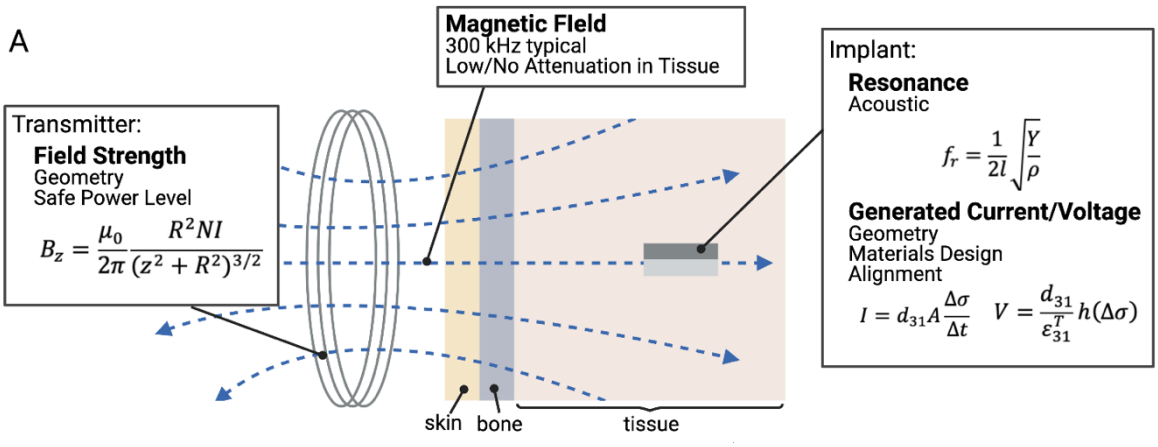

Figure 12 Magnetoelectric wireless power transfer transfers power from an external coil to an implanted magnetoelectric device.

Like ultrasound-powered devices, ME devices also operate under resonant conditions for the piezoelectric material, meaning that they operate at the acoustic resonant frequency with a smaller resonant device size. The resonant frequency was primarily dependent on the length of the implanted film (Equation 8):[84]

$$f_r = \frac{1}{2l}\sqrt{\frac{Y}{\rho}}$$

Equation 8

Here we see the length, l, dependence along with a number of material properties (Y, Youngs modulus, ρ, density). This acoustic resonant condition can be additionally advantageous in comparison with other magnetically powered implants because magnetic fields can be easier to generate and can operate at a much higher safety limit at these lower frequencies.[45]

In addition to the transmitter design (discussed in NIC and RF) and the choice of piezoelectric design (discussed in ultrasound), magnetoelectrics have the added design consideration of the magnetostrictive material, which is characterized by the magnetostrictive coefficient λ. λ is an experimentally measured parameter which compares the fractional change in length with an applied magnetization. The derivative of this curve gives the piezomagnetic coefficient d_{ij} which is the magnetic analog of the previously discussed piezoelectric coefficient.

Maximizing this piezomagnetic coefficient is a combination of two factors. The first is choosing a material with a large change in λ. This may not always be equivalent to choosing a material with a large magnetostriction, because it is the derivative that determines the piezomagnetic coefficient. Secondly, in many cases a bias magnetic field is required because the derivative will be maximized at the inflection point of the magnetostriction curve.[85] Adding in a bias field allows an alternating field to oscillate around that inflection point and generate the maximum possible strain to be transferred to the piezoelectric. The strength of the bias field depends on the material used. Metglas and Terfenol-D are two commonly used magnetostrictive materials in magnetoelectric films.[85–88]

3.2. Fabricating and Characterizing Magnetoelectric Devices

To fabricate ME films, we used Metglas SA1 alloy (Metglas Inc) for the magnetostrictive layer and polyvinylidenefluoride "PVDF" (precision acoustics) or lead Zirconate titanate "PZT" (Piezo Systems) for the piezoelectric layer (**Error! Reference source not found.**). The d_{31} coefficient is 22 pC/N for PVDF (Precision Acoustics) and 320 pC/N for PZT (Piezo Systems) . The PVDF films used for these experiments were pre-stretched and poled by the manufacturer. The two layers were bonded together using an epoxy capable of transferring the mechanical stress between the two layers (Hardman double bubble red epoxy). Prior to bonding the two layers together, we sputtered a thin layer of platinum (<100 nm) as a top electrode on the PVDF. The PZT films are manufactured with a nickel top electrode. Both the Metglas and PVDF were plasma cleaned using O_2 plasma for five minutes before epoxying. After the epoxy set, the films were cut into the desired rectangular

shape using scissors, taking care to cut the long axis of the film along the stretching direction of the PVDF. We then attached wires using conductive epoxy to either side of the films in order to measure the electrical capabilities of the film. We found that attaching wires in the center dramatically increased the resonant voltage. However

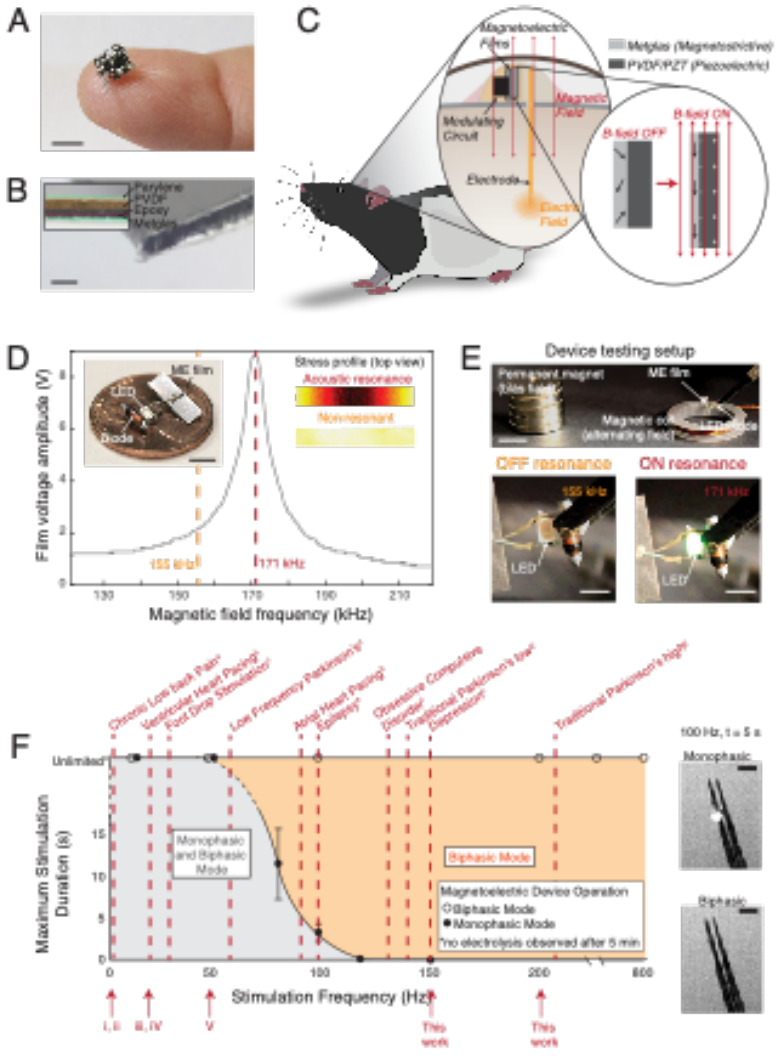

Figure 13 ME films convert alternating magnetic fields into a voltage. (a) Photo of a ME device shown on a fingertip, scale bar=5 mm (b) Cross sectional image of a cut ME film, scale bar=0.2 mm (c) Diagram of a ME device on a freely moving rat for wireless neural stimulation. Inset shows the operating principle whereby strain in the magnetostrictive layer is transferred to the dark grey piezoelectric layer, creating a voltage across the film. (d) Example of a resonant response curve for a ME film where the maximum voltage is produced at an acoustic resonance at 171 kHz. Photograph inset shows an example of an assembled ME stimulator, scale bar=5mm. "Stress profile" inset shows a top view of the stress produced in a ME film as calculated by a finite element simulation on and off resonance (COMSOL). (e) Device testing setup with a permanent magnet to apply a bias field and an electromagnetic coil to apply an alternating magnetic field, scale bars: upper=1 cm, lower=2 m (f) Maximum stimulation duration for a ME device in biphasic and monophasic operation determined by time of electrolysis on a stereotrode in saline as evidenced by gas bubbles (error bars +/- 1 standard deviation for n=4 trials), scale bars=0.2mm. Dashed red lines indicate frequencies of electrical stimulation used in clinical applications, Roman numerals indicate stimulation frequencies demonstrated by previously published miniature magnetic stimulators (i: (Chen et. al. 2015) ii: (Munshi et. al. 2017), iii: (Montgomery et. al. 2015), iv: (Freeman et. al, 2017), v: (Maeng et. al, 2019).

for convenience, the wires were attached near the ends of the films during the in vitro experiments. In many cases we also attached additional electronic components such as diodes or LEDs to the wires attached to the films as noted in the appropriate sections in the main text. Finally the devices were coated in 5-10 μm of parylene-C (Labcoater 2). Initially this coating was used to electrically insulate and protect the devices during in vitro experiments, but we also found that the encapsulation increases the resonant voltage, which could be due to increased mechanical coupling from the encapsulation.

. We used PVDF or PZT layers between 28 and 110 μm, which yielded total device thicknesses between 50-150 μm. We found a dramatic increase in the voltage measured across the film when the applied magnetic field frequency matches an acoustic resonant frequency (Figure 13D). Because the resonant frequency is proportional to the inverse of the film length (Figure 14 I), we can design multiple films and selectively activate them by changing the stimulus frequency. Using this principle, we can use different magnetic field frequencies to activate separate monophasic devices that may be in different areas of the body, or create biphasic stimulators by interleaved resonant stimulation of two different films, with each film driving either the positive or negative phase of the neural stimulus.

We can further enhance the voltage generated by the films by applying a constant bias field with a permanent magnet or an electromagnet (Figure 13 E). Because the strain in the magnetostrictive material is a sigmoidal function of the magnetic field

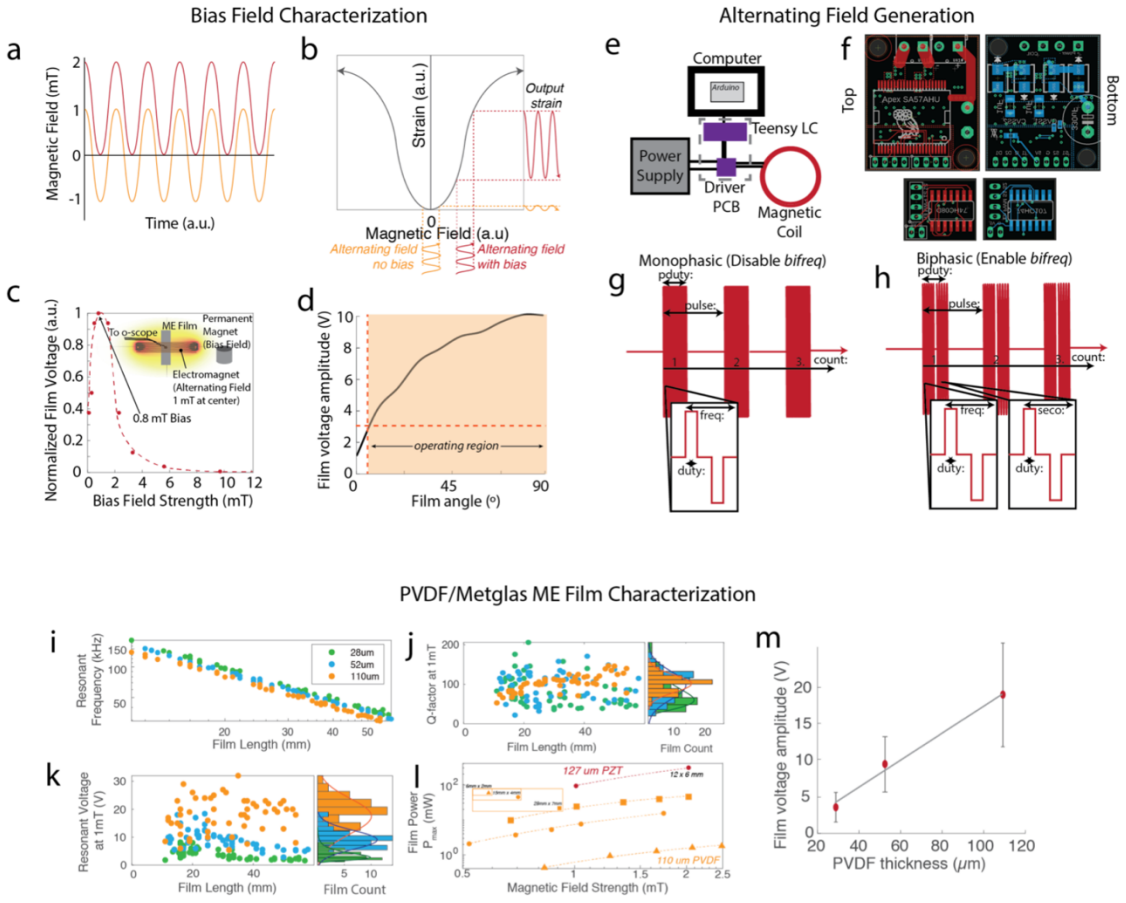

Figure 14 Magnetic Field and Film Characterization, Related to Figure 1 (a) The magnetic field used at the location of the film in every experiment is the combination of a bias field and an alternating field (b) This maximizes the strain in the magnetoelectric material (c)The peak resonance voltage is significantly increased by a modest bias field that can be produced by a permanent magnet (d) The ideal orientation of the films is parallel with the field direction however, operation is still possible even with misalignment due to the high initial voltage (e) Schematic of the major components of the magnetic field driver. Circuit diagrams for the driver PCBs shown in (f). (g) Output waveform for monophasic stimulation and the parameters that can be controlled by the drive software (h) Output waveform for biphasic stimulation, and the parameters that can be controlled by the driver software (i) As film length decreases the resonant frequency increases but the q-factor (j) and output voltage (k) remain the same. (l) The output power depends on the film area and material, while the voltage depends on the thickness of the piezoelectric layer (m).

strength, the change in voltage produced by the alternating field is largest when the field oscillates about the midpoint of the sigmoid (Figure 14 A-C).[85,89] Thus, we use a

bias field (approximately 8-9 mT for devices used here) to offset the alternating magnetic field near the center of the sigmoidal magnetostrictive response curve. Our references to magnetic field strength in this work refer to the amplitude of the alternating magnetic field around this bias point.

To identify safe operational conditions for our ME stimulators we tested them using a stereotrode (Microprobes) in saline over a range of frequencies. The ME stimulator was wired to a stereotrode immersed in saline under a microscope in order to observe the formation of bubbles from electrolysis at the tips. During monophasic stimulation we used only one resonant frequency (one film) and during biphasic stimulation we used two frequencies (two films). In each case the pulse time was a 400 μs/phase. We determined the limit of stimulation time as when the first bubble began to appear at the tips of the electrode and repeated each data point 4 times. We found that a biphasic stimulation waveform allowed us to apply constant stimulation up to at least 800 Hz without hydrolysis and monophasic stimulation could be safely applied up to approximately 50 Hz. For these tests we used stimulation amplitude of 2 V and duration of 400 μs/phase (which is common for in vivo experiments). The safe ranges were determined by measuring the time at which we could see bubbles at the electrode tip (Figure 13F) resulting from hydrolysis, which indicates conditions that would lesion tissue. Compared to previously demonstrated miniature magnetic neural stimulators that operated in a monophasic stimulation mode, the biphasic ME devices shown here can access the high frequency bands used for clinical applications like the treatment of Parkinson's disease and obsessive-compulsive disorder (Figure 13 F, References a[90], b[34], c[91], d[92], e[93], f[94], g[95], h[96]). The ME devices can also operate safely in a monophasic mode for low-frequency applications such as heart pacing or chronic pain stimulators, which can be achieved with a simplified ME device. One should note that the exact safety windows depend on the amplitude, duty cycle, and electrode configuration of the stimulator.

An additional challenge for any wirelessly powered neural stimulator is to maintain a well-regulated stimulation voltage, especially as devices become small and the power transfer efficiency is reduced. ME materials offer two main advantages that can enable stable and effective stimulation as devices become small and move with respect to the driver coils:

First, ME devices generate voltages in excess of the effective stimulation potential, allowing them to be effective even if the materials are misaligned with the driver coils. At resonance, we have measured open-circuit ME voltages in excess of 30 V at a field strength of only 1 mT (Figure 14K,M). Because effective stimulation voltages are usually between 1-5 V, we can cap the applied voltage to this effective stimulation range using an LED or Zener diode. As long as the voltage generated by the ME film is greater than or equal to the capping voltage, our device could apply the same stimulus voltage regardless of the angle or distance between the driver coil and the ME film. For a typical film we found that we could reorient the film by +/- 80 degrees and maintain voltages in excess of 3 V (Figure 14D). This large angular tolerance is aided by the large magnetic permeability of the Metglas layer, which helps to direct the magnetic field lines along the long axis of the film, where they are most effective at creating a magnetostrictive response.

Second, the voltage generated by a piezoelectric material depends on the thickness and not the area of the piezoelectric layer[73], allowing us to fabricate small magnetoelectric films that generate roughly the same stimulation voltage as larger devices. Figure 14 J,K shows the peak voltage generated and quality factor for ME films of different areas. We found that, for a 52 μm thick PVDF layer, the voltage remains around 10 V even as the film length decreases. Variations of +/- 40 % in peak voltage and quality factors are likely due to defects produced during film fabrication, which may be reduced with improved manufacturing. We also verified

that the output voltage depends only on the piezoelectric film thickness by measuring the peak voltages from ME devices with three different thicknesses of PVDF: 28 μm, 52 μm, and 110 μm. As expected, we see that the peak voltage increases linearly with the PVDF thickness and is independent of the film length.

For applications such as current delivery through implanted electrodes, where the available power is an important figure of merit, the advantage of our ME technology is the power we get from a mm-sized magnetically powered device. This allows us to perform experiments that require high power like high frequency biphasic stimulation. Our calculations and experimental data show that the power generated by a ME device is proportional to the film area for a given thickness and a length-to-width ratio >3 (see Figure 14 L). This output power is also dependent on the d_{31} coefficient of the piezoelectric material (Figure 14). Despite the decrease in power as films become smaller, we calculate that PVDF/Metglas films less than 10 mm long can generate up to 4 mW, which is sufficient for many wireless applications including neural stimulation.[97] In applications requiring higher power at miniature scales, we use PZT/Metglas ME films due to the higher d_{31} of PZT.

Chapter 4

Demonstrating Magnetoelectrics for Neural Modulation[20]

4.1. Monophasic stimulation by ME films modulates cellular activity in vitro

Using fluorescence microscopy to image voltage in cultured cells, we found that monophasic stimulation directly from PVDF/Metglas ME films reliably stimulated action potentials (APs). For these experiments we used "spiking" human embryonic kidney (HEK) cell lines that were modified to express sodium and potassium channels (see Methods). These cells have spike-like electrical waveforms that are rectangular in shape and can last for a few seconds depending on the confluency of the culture [98]. To determine the relative timing between magnetic stimulation and AP generation, we transfected these cells with ArcLight -a genetically encoded voltage indicator[99].

To image fluorescence while we applied magnetic fields, we developed an experimental setup that allows us to place cells and ME films beneath an objective lens at the center of a 10 cm long solenoid with a 3 cm gap in the center (Figure 15A). The field strengths (<1 mT, Figure 16F) and frequencies (20-40 kHz) used in this

experiment did not produce noticeable heat in our metallic objective lens or interfere with our imaging. Two slightly larger coils placed on either side of the gap provided the constant bias field.

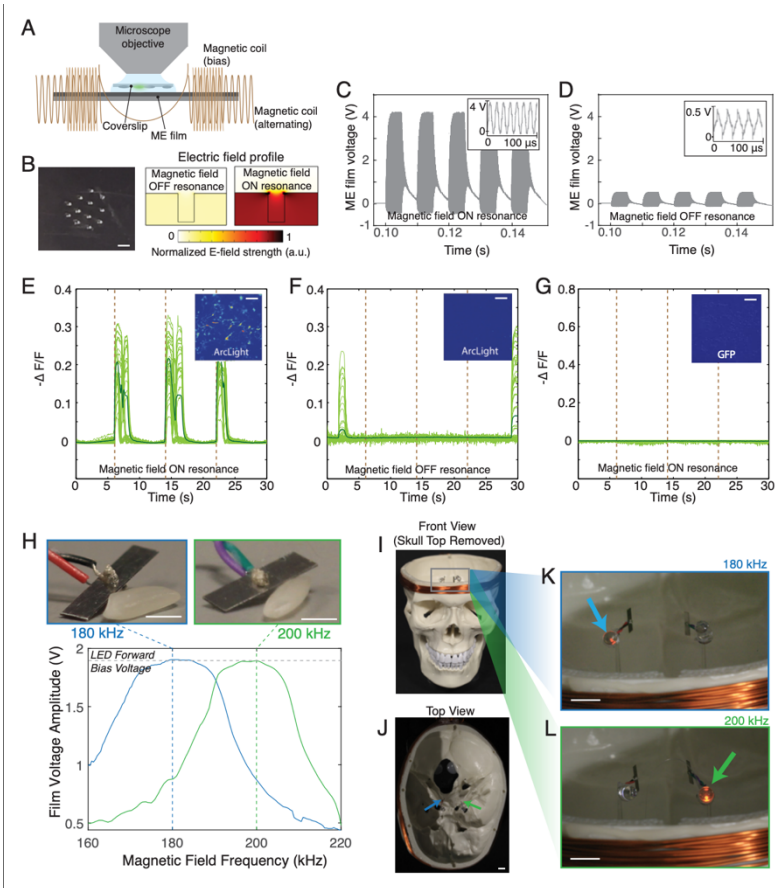

Figure 15 Monophasic ME stimulators activate cells in vitro (a) Schematic of the experimental setup (b) Microscope image of holes stamped into the ME film, scale bar=0.5mm, and finite element simulation of the electric field shows fringing electric fields that overlap the culture cells (c) Voltage across the ME film when the magnetic field is on resonance and (d) off resonance. Insets show a zoom in of the high frequency carrier waveform. (e-g) Fluorescence from spiking HEKs transfected with ArcLight show action potentials are triggered by the ME film driven at resonance (e), but not when the film is driven off resonance (f). Fluorescence from HEK cells transfected with GFP (g) show no response when the ME film is driven on resonance, scale bars=0.2mm (h) Photos of miniature ME films next to a grain of rice and the corresponding voltage as a function of magnetic field frequency (field strength 0.5 mT, scale bars 2 mm) (i) Front view and (j) top view of skull phantom with the top removed to view LEDs (film locations indicated by arrows, scale bar 1 cm (k) Photo of LEDs attached to ME films with the magnetic fields at applied at 180 kHz and (l) 200 kHz. Selective illumination of the LEDs corresponding the resonant frequencies of the films demonstrates successful multichannel activation of individual films, scale bars 1 cm. See also Fig. 16 Video S1

We then approximated an implanted ME stimulator using two experimental configurations: 1) growing cells directly on the ME film (Figure 16) and 2) inverting a coverslip with adherent cells on top of the ME film (Figure 15) because in a typical use case, the target cells may not adhere to the ME stimulator (see Methods).

To create fringing electric fields that interact with the cultured cells, we stamped holes in the ME film (Figure 15B). The films were otherwise fabricated as described previously. In experiments using ME films and Pt electrodes we found that high-frequency biphasic stimulation at the ME resonance frequency (typically 20-150 kHz) was not effective to stimulate APs in cultured HEKs, as predicted by the low-pass filtering properties of the cell membrane.[100] To create an effective monophasic stimulus waveform, we used a diode to rectify the voltage to generate a waveform that has a slowly varying monophasic envelope in the <500 Hz frequency band where cells are responsive (Figure 15C,D).

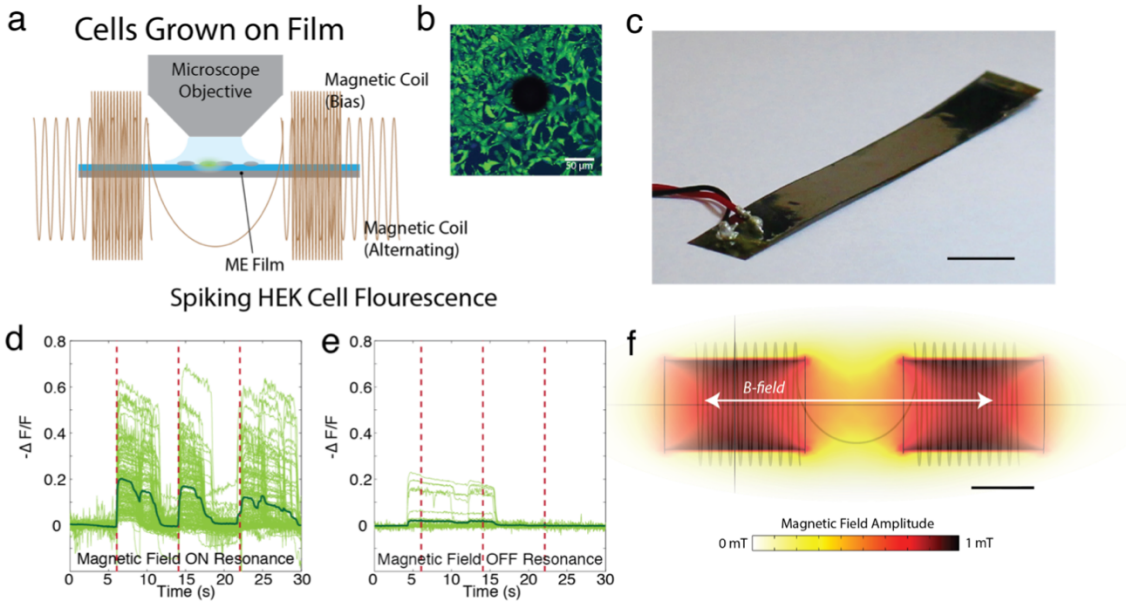

Figure 16 ME films in vitro, (a) Schematic of experimental setup for testing cells grown on ME films (b) Microscope image of fixed cells adherent to the region around a stamped hole (Hoechst/Calcein-AM, cells labeled prior to fixing) (c) sample film used for in vitro testing (scale bar = 4 mm) (d) ArcLight fluorescence of spiking HEK cells when magnetic field is on resonance and (e) off resonance (f) COMSOL simulation of the magnetic field strength used in this experiment (scale bar = 3 cm)

For cells grown directly on the ME films and those placed in contact we found that five stimulation pulses with an envelope frequency of 100 Hz (applied for only 50 ms total so as not to introduce hydrolysis) consistently stimulated APs in the spiking HEK cells (Figure 15E, Figure 16D, Supplementary Video 1). Critically, this stimulation frequency is within the therapeutic window for many deep brain stimulation treatments,[101] and difficult to achieve with other wireless stimulators that compensate for low-efficacy energy harvesting by charging on-board capacitors.[51] For our experiments, the carrier frequency of the magnetic field was at the resonant frequency of the film (Figure 16C). To test stimulation reliability, we repeated the 5-pulse stimulus three times over a period of 30 seconds. We observed APs for each stimulation pulse in n = 43 cells on coverslips and n = 144 cells grown on films. In these experiments all cells in the field of view were activated simultaneously due to the fact that HEK cells are known to be electrically coupled when grown to confluence [98]. We confirmed that the APs stimulated by the ME film were in fact the result of resonant excitation of the film and not an artifact of the applied magnetic fields by imaging voltage-sensitive fluorescence when the magnetic field was tuned off of the resonant frequency. For non-resonant excitation we observed no correlation between the applied field and fluorescently detected APs in the spiking HEKs (Figure 15F, Figure 16E), supporting the conclusion that APs were stimulated by the ME film at resonance. We also confirmed that the fluorescent signal recorded represents the voltage-dependent ArcLight response by imaging cells transfected with voltage-independent cytoplasmic GFP. These cells showed no change in fluorescence when the films were driven at the resonant frequency (Figure 15G).

4.1.1. ME devices can be individually addressed based their resonant frequency

Another advantage of ME technology is that we can individually address multiple miniature implanted devices by fabricating the films to have unique resonant frequencies. As a demonstration we show that two rice-sized ME films with cross sectional areas of ~16 mm^2 can be individually addressed at the center of a human skull phantom using an external electromagnet. These films with lengths of 8 mm and 10 mm have resonant frequencies of 180 and 200 kHz (Figure 15H). When they are attached to an orange LED, their output voltage is capped at 1.8 V, which allows us to regulate the stimulation voltage and visualize film activation. ME films of this size are smaller than current DBS leads and could potentially be implanted into deep brain areas as shown in Figure 15I-L. Additionally, the magnetic coil is small enough to be incorporated into a stylish hat that could be worn by a patient. When we placed the two ME films at the center of a skull phantom we could individually light the LEDs on each film when we applied a magnetic field (0.5 mT at the center of the skull phantom) at the resonant frequency of the selected film (Figure 15I-L). The skull top was removed for visualization, but had no effect on our ability to drive the LEDs. The number of stimulation channels could be increased with the addition of ME films with different resonant frequencies.

4.1.2. Methods

In Vitro HEK Experiments

For experiments performed on coverslips, HEK cells expressing sodium channel $Na_{1.3}$ and potassium channel $K_{2.1}$ were grown on 12 mm poly-l-lysine coated coverslips to approximately 30% confluency. The cells were then transfected with the genetically encoded voltage indicator ArcLight using Lipofectamine (Invitrogen)

following manufacturer's recommendations. Two to three days after transfection the coverslips were inverted onto ME films for testing. Preparation of GFP controls followed the same procedure with the exception of replacing the ArcLight vector (AddGene) with a GFP expression vector (AddGene). For experiments performed with cells grown on the films, HEK cells transfected with ArcLight were placed onto parylene coated poly-l-lysine treated films. The films were placed in cellular media overnight and tested the following day. The healthy proliferation of HEKs on the ME device indicates that this encapsulation approach prevents the ME materials from limiting cell growth (Figure 16B).

ArcLight and GFP were excited at 460 nm with an LED light source. Fluorescence images were collected at 33 fps using a CCD camera. Images were analyzed using Matlab to quantify fluorescence changes in individual cells. In vitro testing was performed in extracellular buffer (ECB, in mM: NaCl 119, KCl 5, Hepes 10, $CaCl_2$ 2, $MgCl_2$ 1; pH 7.2; 320mOsm)

Figure S2b was obtained by growing unmodified HEK cells on a film submerged in cellular media for five days. The cells were then stained with Hoechst and Calcein-AM to label the nucleus and membrane respectively in living cells. The cells were then fixed and imaged using a confocal microscope.

Skull Phantom Demonstration

At the magnetic field frequencies used for this experiment bone and tissue are effectively transparent, [102]so we selected a life sized skull with the size of an average human adult head as a phantom (Orient Infinity Limited). It was wrapped with 18 AWG magnet wire as shown in Figure 15. The coil consisted of four coils in parallel each wired to an individual magnetic field driver. All drivers were wired to the same input frequency signal and powered from the same power supply. The films were suspended at the center of the skull phantom. Orange LEDs (Chanzon)

with a diode antiparallel were attached to the films for wireless verification of the voltage generated by the films. For visualization purposes the skull top was removed to better photograph the LED.

4.2. Biphasic stimulation from ME films can drive high-frequency neural activity ex vivo

Biphasic stimulation is used for most biomedical stimulators because its charge-balanced waveform reduces charge buildup and undesired electrochemical reactions at the electrode surface.[103] To create an effective biphasic stimulus in the therapeutic window (100 – 200 Hz), we use two films with distinct resonant frequencies connected to the same stimulating electrodes (Figure 17A,C). By switching the magnetic field frequency between the two resonant frequencies, we can alternate positive and negative phase stimulation to create a biphasic neural stimulator (Figure 17D,E). In this case the residual charge of <1 nC, which discharges in <2 ms, implies that this stimulator can safely operate at frequencies up to >500 Hz without accumulating charge.

We demonstrated that clinically relevant regions of high frequency stimulation are safely accessible with this ME powered device by using our biphasic ME stimulator to drive high-frequency neural spikes in a mouse brain slice (see Methods). We stimulated axons of thalamic reticular nucleus (TRN) neurons by placing a stereotrode attached to the ME stimulator into the adjacent ventrobasal nucleus of the thalamus and performing whole-cell voltage-clamp recordings in TRN neurons (Figure 17A). We found that short-latency antidromic spikes were reliably evoked (Figure 17B), with the recorded spike frequency matching the programmed magnetic field envelope frequency (10, 50, and 150 Hz) confirming that neuronal activity can be precisely controlled using our ME stimulation (Figure 17F-H).

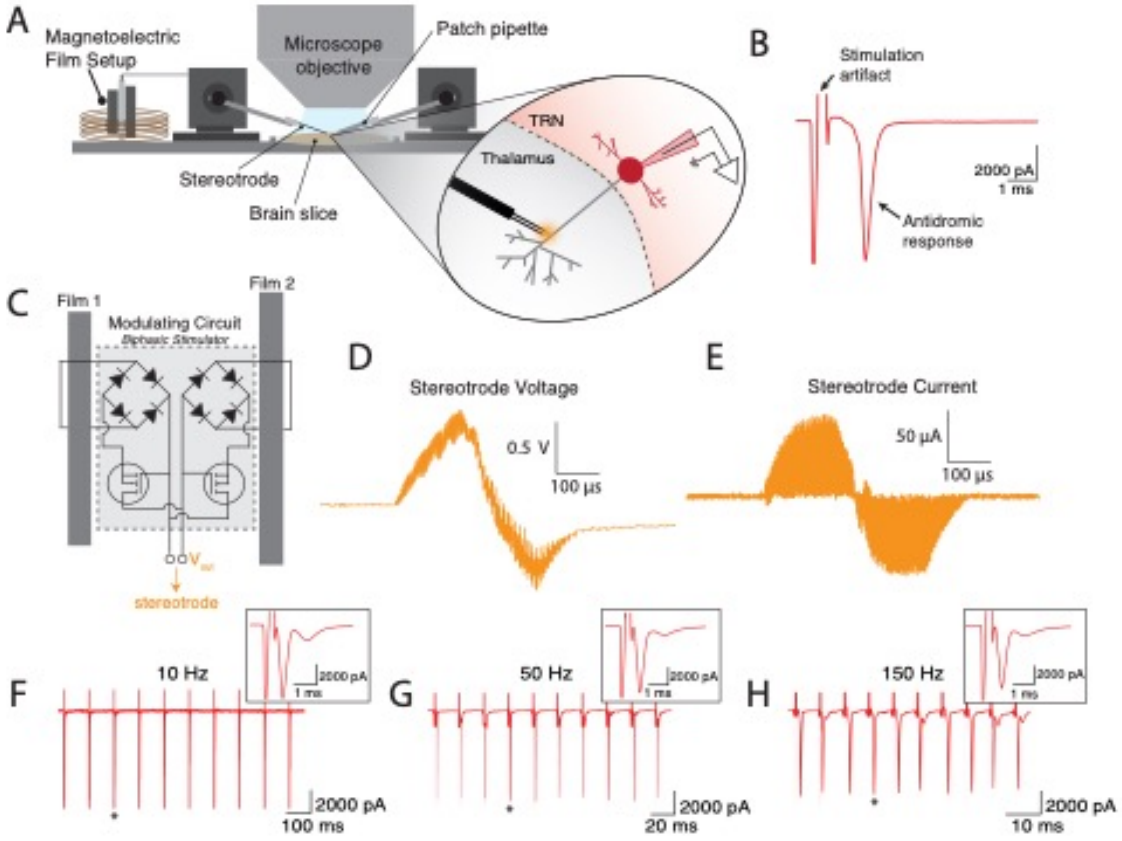

Figure 17 Biphasic ME stimulators activate neurons in ex vivo brain slices (a) Schematic of experimental setup with two ME films for biphasic stimulation. A bipolar stereotrode was placed into the ventrobasal nucleus of the thalamus to activate axons of TRN neurons (b) Representative voltage-clamp recording in TRN showing stimulation-triggered short-latency antidromic spike (artifact cropped for scale). (c) Schematic of the circuit used to generate the biphasic waveform (d) Measured voltage across the stereotrode shows the biphasic pulse shape (e) Calculated current based on measuring the voltage across a load resistor shows nearly perfect charge balancing with <1 nC accumulating on the electrode per pulse train. (f-h) Recorded spike activity at various frequencies of ME stimulation demonstrates the ability of the ME device to reliably entrain action potential activity at 10, 50, and 150 Hz (stimulus artifacts cropped for clarity) insets show zoom in of individual antidromic spikes.

We also found that our biphasic ME stimulator is capable of repeatable neural stimulation using neocortical brain slices derived from mice that express the genetically encoded calcium indicator GCaMP3 in glutamic acid decarboxylase 2 (GAD2) positive GABAergic neurons (Figure 18). To record neural activity following

ME stimulation we again inserted a stereotrode attached to the biphasic ME stimulator described above and imaged local GCaMP fluorescence increases using a 60x water immersion lens (Figure 18A-C, Methods). Due to the background fluorescence and scattering we observed only overall fluorescence changes in the field of view (300 x 300 μm) which contains up to 100 GCaMP3 positive neurons that could contribute to the observed signal.[104] We chose neural stimulation parameters of 100 biphasic pulses at 200 Hz with each

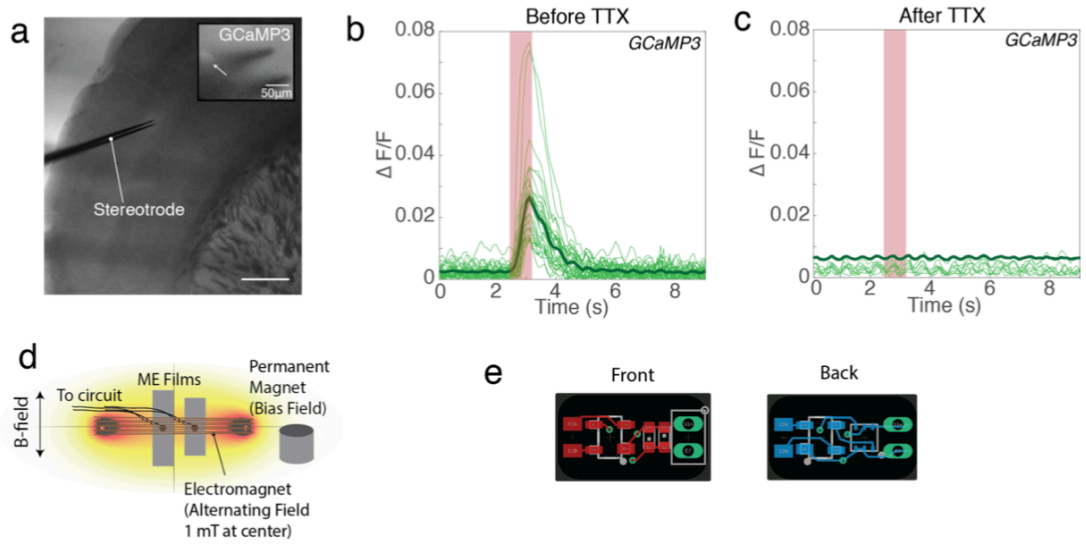

Figure 18 Additional Brain Slice Experiments (a) Bright field image of stereotrode in mouse cortex (scale bar = 400 μm), with inset showing GCaMP fluorescence around stereotrode tip. Arrow indicates a fluorescent cell body. (b) Imaging of neural activity induced by the ME stimulator. Recordings were obtained from a 300x300 μm area using a 60x water immersion lens. Shown are time-locked GCaMP fluorescence increases following application of resonant magnetic field. (c) TTX application eliminates all fluorescence transients. Thin traces in (b) and (c) represent separate experiments from two brain slices, and thick traces represent the mean of all experiments. (d) Magnetic field setup used in this setup and (e) circuit board used in this experiment

phase lasting 175μs. When the magnetic field was on we observed a corresponding increase in fluorescence in neocortical layer 5 (n=23 recordings obtained in 2 brain slices) consistent with stimulus-evoked calcium increases in local neurons.

Following bath application of tetrodotoxin (TTX, 500 nM) fluorescence increases were completely blocked in n=9 recordings confirming that ME evoked calcium increases were dependent on action potentials. Positive results in both slices analyzed were sufficient to qualitatively confirm that neurons were reliably activated by our ME stimulator.

4.2.1. Methods

Brain slice experiments:

All experiments were performed in accordance with NIH guidelines and approved by the University of Texas Health Science Center at Houston (UTHealth) animal welfare committee. For electrophysiology, we used 16-day-old C57BL6/J mice (JAX #000664). For GCaMP imaging we used 40 day old GAD2-GCaMP3 mice, generated by crossing GAD2-Cre (JAX # 10802) with flox-GCaMP3 (JAX # 14538) animals.

Electrophysiology

We prepared thalamocortical brain slices (400 μm) as described previously.[105] Briefly, wildtype mice were anesthetized and decapitated, in accordance with NIH guidelines and approved by the University of Texas Health Science Center at Houston (UTHealth) animal welfare committee. Brains were removed and immediately transferred to an ice-cold sucrose-based cutting solution containing (in mM): 234 sucrose, 2.5 KCl, 1.25 NaH_2PO_4, 10 $MgSO_4$, 0.5 $CaCl_2$, 26 $NaHCO_3$, and 11 glucose, saturated with 95% O2, 5% CO_2. Slices were cut using a vibratome (Leica VT 1200S) and transferred to ACSF containing (in mM): 126 NaCl, 2.5 KCl, 1.25 NaH_2PO_4, 2 $MgCl_2$, 2 $CaCl_2$, 26 $NaHCO_3$, and 10 glucose. Slices were held at 35°C for 20 min and then kept at room temperature until used for recordings. For experiments, slices were placed in a recording chamber and perfused with ACSF

held at 31-34°C and containing NBQX (R&D Systems) to block AMPA receptor-mediated synaptic transmission. Whole-cell voltage-clamp recordings from neurons in the thalamic reticular nucleus (TRN) were performed using glass pipettes (3-5 MΩ) filled with a potassium based internal solution containing (in mm): 133 K-gluconate, 1 KCl, 2 $MgCl_2$, 0.16 $CaCl_2$, 10 HEPES, 0.5 EGTA, 2 Mg-ATP, and 0.4 Na-GTP (adjusted to 290 mOsm, pH 7.3). Antidromic action potentials were evoked by placing stereotrodes in the adjacent ventrobasal nucleus of the thalamus. Data were acquired using a Multiclamp 700B amplifier (Molecular Devices), filtered at 10 kHz, and digitized at 20 kHz with a 16-bit analog-to-digital converter (Digidata 1440A; Molecular Devices).

GCaMP Imaging

Brain slices were prepared closely following procedures described previously.[106] GAD2-GCaMP3 mice were deeply anesthetized with Isoflurane and perfused with ice cold NMDG-based solution consisting of (in mM): 92 NMDG, 2.5 KCl, 1.25 NaH_2PO_4, 10 $MgSO_4$, 0.5 $CaCl_2$, 30 $NaHCO_3$, 20 glucose, 20 HEPES, 2 thiouera, 5 Na-Ascorbate, 3 Na-pyruvate, saturated with 95% O_2 and 5% CO_2., at a rate of ~6 ml/min. Coronal brain slices (300 μm) were cut using a vibratome (Leica VT1200S), incubated for 15 min at 35 °C in NMDG-based solution, and then transferred to a chamber held at room temperature containing (in mM): 92 NaCl, 2.5 KCl, 1.25 NaH_2PO_4, 2 $MgSO_4$, 2 $CaCl_2$, 30 $NaHCO_3$, 25 glucose, 20 HEPES, 2 thiouera, 5 Na-Ascorbate, 3 Na-pyruvate, saturated with 95% O_2 and 5% CO_2. For experiments, slices were placed into a recording chamber perfused with ACSF containing (in mM): 126 NaCl, 2.5 KCl, 1.25 NaH_2PO_4, 2 $MgCl_2$, 2 $CaCl_2$, 26 $NaHCO_3$, 10 glucose), held at 32-34 °C. The AMPA receptor antagonist NBQX (10 μM) was included in the bath solution to synaptically mediate network activity. Stereotrodes were placed in layer 5 of somatosensory (barrel) cortex. GCaMP3 expressed in GAD2 positive GABAergic neurons was excited at 460 nm with an LED light source. Fluorescence

images were collected at 9.8 fps using a CCD camera attached to an Olympus BX51WI microscope equipped with a 60x water immersion objective. Images were analyzed using Matlab to quantify fluorescence changes from a 300 x 300 μm region around the stereotrode tips.

4.3. ME Neural Stimulation in Freely Moving Rats Provides Therapeutic Benefit

A major advantage of our ME stimulators is that remote activation enables experiments with freely behaving animals. As a proof-of-principle we adapted our biphasic stimulator for deep brain stimulation (DBS) in freely moving rats (Figure 19). To test ME stimulator efficacy, we used a previously reported protocol to test DBS in hemi-parkinsonian rats.[107] In these experiments rats are injected with 6-OHDA in the left medial forebrain bundle (MFB) to create a unilateral lesion of the substantia nigra pars compacta (SNc). The animals are then placed in a 30 cm diameter circular enclosure. Following a dose of methamphetamine, the hemi-parkinsonian rats have been shown to rotate ipsilateral to the injection (e.g. left for injection into the left MFB). During these rotations, the rat primarily moves using its contralateral (right) forepaw, rarely placing the ipsilateral (left) forepaw onto the ground. When a biphasic stimulus is applied at 200 Hz in the sub-thalamic nucleus (STN) using a tethered electrode array stimulator, rats typically stop turning to the left and exhibit more normal behavior such as moving with both forepaws, maintaining a steady orientation, or turning to the contralateral side.[101]

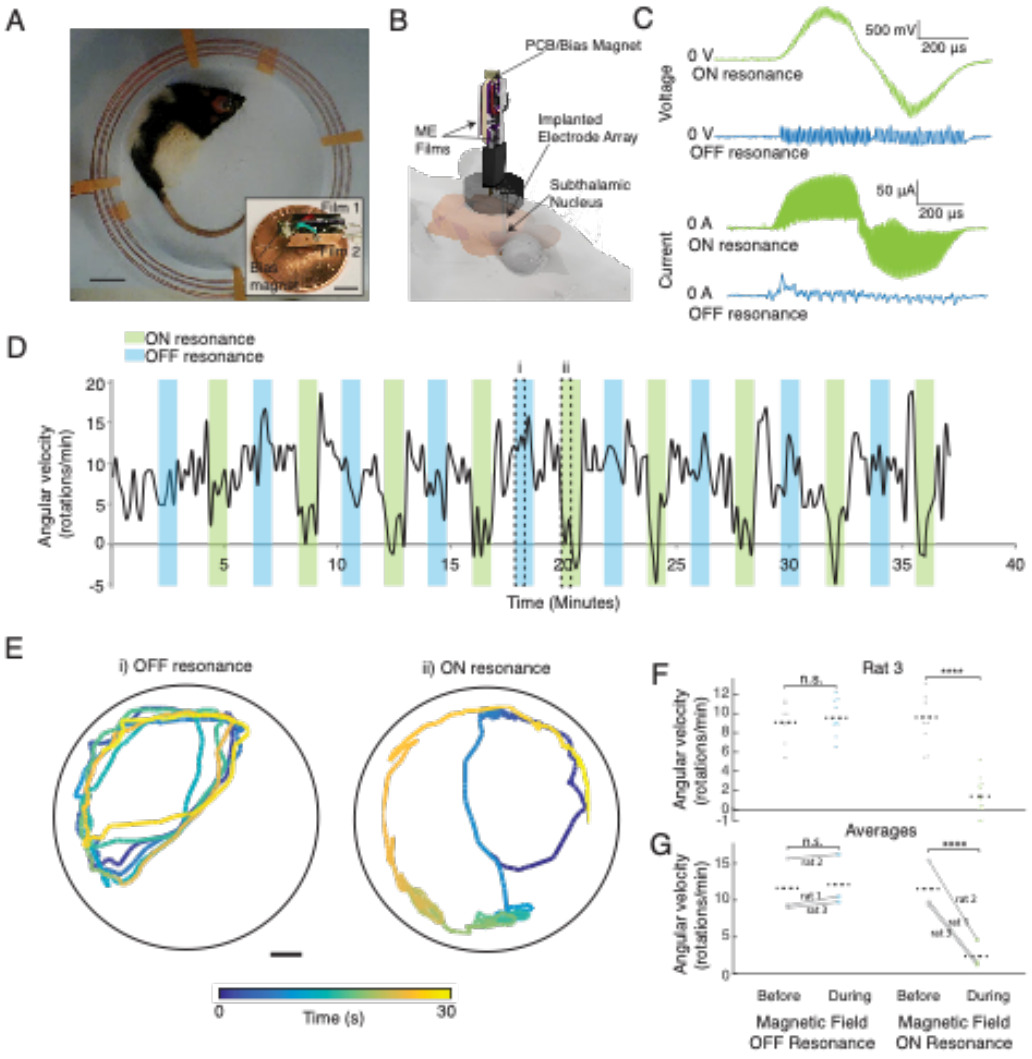

Figure 19 Effective DBS in a freely moving rat using a wireless ME stimulator (a) Experimental setup showing rat in a circular enclosure wrapped with a coil, scale bar=5cm. Inset shows a biphasic ME stimulator on a one cent coin, scale bar=5mm (b) Schematic of the biphasic ME stimulator attached to the electrode array implanted into the STN (c) Measured voltage generated by the ME device and the current applied to the brain on resonance (green) and off resonance (blue) (d) Angular velocity of the hemi-Parkinsonian rat over a 40 minute trial with intervals of resonant and non-resonant stimulation, showing reduced rotations when the stimulator is activated on resonance (e) Typical trajectories show the location of the animal's head over two 30-second intervals denoted in c, scale bar = 5cm (f) Average angular velocity of the rat during the 30 seconds before stimulation and the first 30 seconds of stimulation for each interval during the 40-min experiment (** P = 4x10-7, n.s.=not significant P=0.70, paired t-test) (g) Average angular velocities for n=3 rats shows repeatable results across animals (**** P = 2.8x10-18, n.s.=not significant P=0.11, paired t-test) See also Fig. S4 and Videos S3 and S4**

To create a wireless, biphasic ME stimulator for freely moving animals we added a small permanent magnet (<0.25g) to the ME stimulator to generate a bias field as the animal moved, and wrapped the behavioral chamber with wire to create a solenoid for the alternating magnetic field (Figure 19A, Figure 20). This 0.5g ME stimulator was then connected to a commercial electrode array (Microprobes) implanted in the STN (Figure 19B, see Methods). We ensured that the stimulation voltage and current were within the safe and therapeutic range by measuring the output of the ME stimulator connected to an equivalent circuit model of the brain (Figure 19C, see Methods). Specifically, we observed peak voltages of approximately +/-1.5 V and peak currents of approximately +/- 100 μA for 400 us at approximately a 50% duty cycle (200 μs of overall current per phase), which is within the effective stimulation range reported for conventional wired stimulators.[107] When we tune the magnetic field frequency off resonance we observe almost no generated voltage or current (Figure 19C).

We then tested our wireless biphasic ME stimulator mounted to the head of a rat and found that ME stimulation showed efficacy comparable to previously reported wired DBS stimulators (Figure 19). With a magnetic field applied at resonance, we found that one-minute periods of 200 Hz biphasic pulses resulted in a significant decrease in the animal's rotation rate (Figure 19D green intervals). This decreased rotation was not observed when the magnetic stimulus frequency was tuned off resonance (Figure 19 D blue intervals). Plots of the head trajectories show that the pathological ipsilateral rotations observed during off-resonant magnetic field stimulation are not present when the ME stimulator is active during resonant magnetic field stimulation where the rotations are either not present or contralateral as expected for successful stimulation (Figure 19E, Supplemental Video 2,3, Methods). When averaged over all trials, average rotation rate during the first half of stimulation fell to a statistically significant 1.4 rotations per minute (rpm),

compared to 9.4 rpm in the absence of stimulation, or 10.6 rpm during off-resonant stimulation (paired t-test,

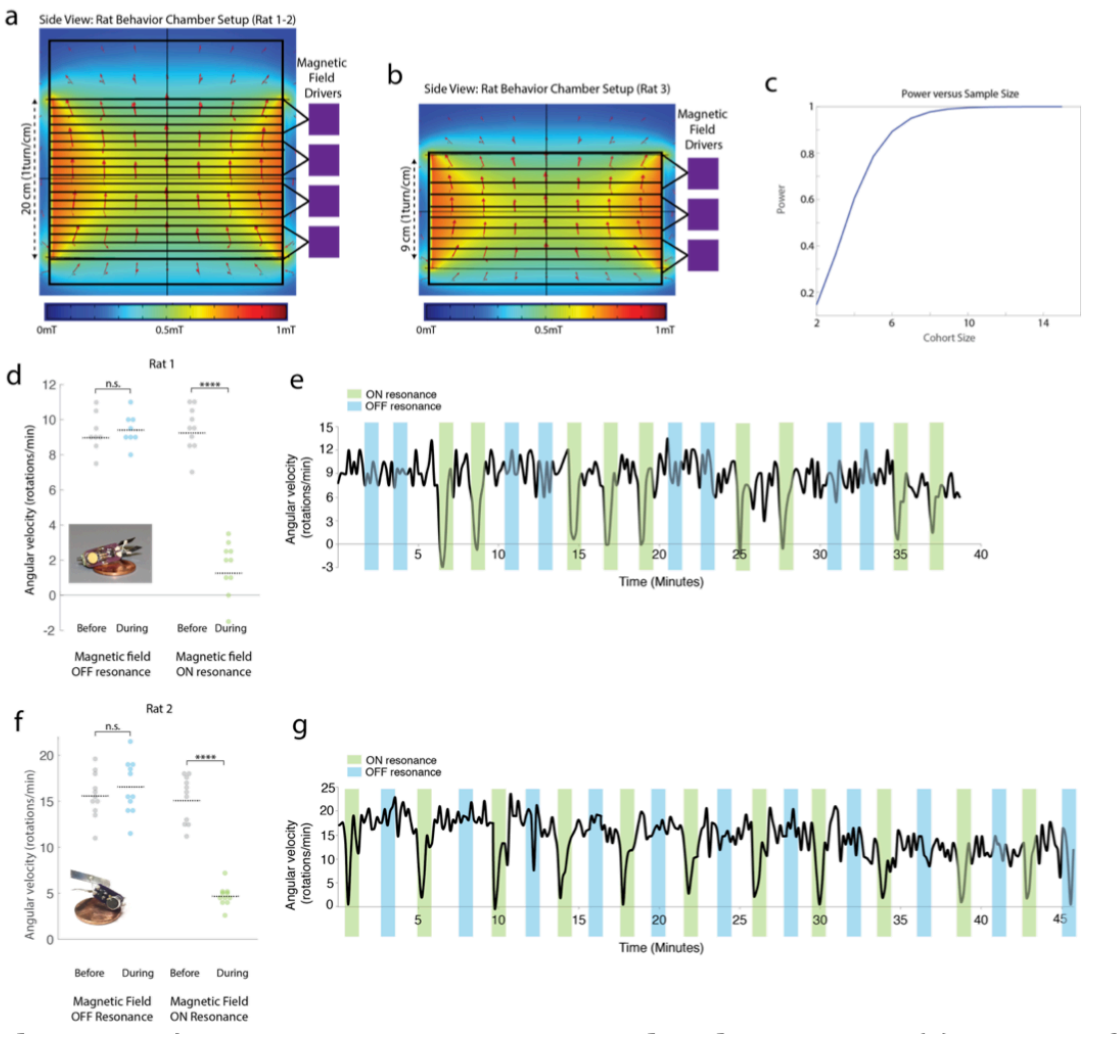

Figure 20 DBS Rotation Experiment (a) Magnetic field setup used in rats 1-2(a) and rat 3(b). (c) Suggested power vs sample size for future neuroscience results where power should be >0.8 (d-f) Change in angular velocity for rats 1 and 2 over an ~40 minute trial of resonant and non-resonant magnetic fields, insets show the ME device used

Figure 19F). We further demonstrated the repeatability of these results by repeating this stimulation protocol on two other rats and found similar results (Figure 19G, Figure 20). A power analysis based on our proof-of-concept data suggests that future

neuroscience experiments using this technology for hypothesis testing would require larger cohorts of approximately 6 rats (Figure 20C).

4.4. Millimeter-sized ME devices enable fully implanted biphasic stimulation in freely behaving rodents

By miniaturizing the components of our stimulator, we created a fully implanted version of our biphasic stimulators (Figure 21). This biphasic device is composed of two mm-sized ME films (4.3 mm x 2 mm, and 5.4 mm x 2 mm in area) connected with circuit elements described previously (Figure 21B) and wired to a stereotrode. We packaged the device using a 3-D printed plastic shell coated in epoxy to protect the films and circuit from the surrounding biological environment (Figure 22B). This miniature design enabled the films and circuitry to be placed on the skull of the rat with the skin sutured up over the implant (Figure 21A,E), which could help prevent issues arising from percutaneous leads.

We performed a place preference experiment to demonstrate that this fully implanted device effectively stimulates neural activity in a freely moving rodent. Because this experiment requires higher stimulation currents than the DBS experiment, we replaced the PVDF piezoelectric layer with PZT (Figure 21C). We then implanted the device connected to a stereotrode surgically placed in the medial forebrain bundle (MFB), which is part of the reward pathway commonly used to drive behavior.[19] One to three days following surgery we placed each rat (n = 3) on a linear track with two custom-designed double resonant coils at either end of the track. For each experiment the coil at one end for the track was ON resonance for both of the implanted films and coil at the other end of the track was OFF resonance. To test for any confounding effects of the magnetic field, we ensured that each coil

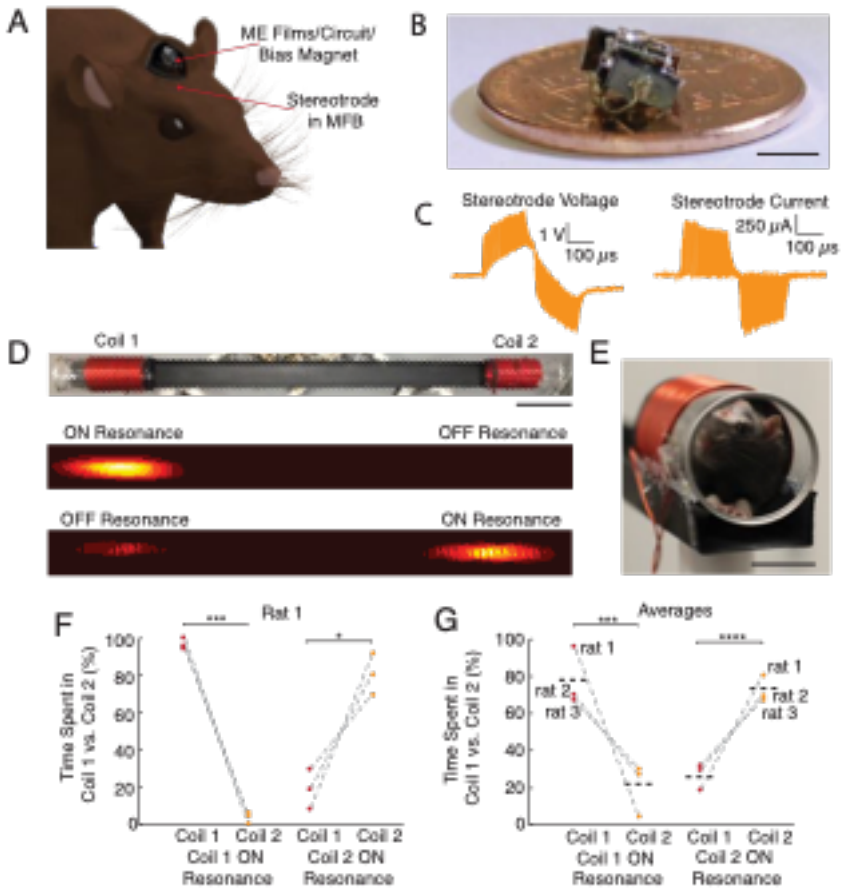

Figure 21 Fully implanted ME device stimulates place preference in freely moving rats (a) Schematic of the device implanted under the skin of a rat with stereotrode implanted into the MFB (b) Inner circuit and films used in the implant, scale bar=5 mm (c) Representative voltage and current waveforms used for stimulation (d) Experimental setup of the linear track and representative heat maps for two individual trials showing a preference for the ON resonance coil showing we could change the preference by altering the frequencies in each coil, scale bar=10 cm (e) side view of the setup showing a rat in the coil with the skin sutured over the implant, scale bar=3cm (f) Preference results from one rat over six trials (*P = 9x10-4, *P = 0.038) and (g) Average results for n=3 rats shows repeatability across animals (***P = 2.7x10-4, ****P = 3.6x10-5) See also Fig. S5 and Video S5**

produced the same field strength of 1.5 mT (Figure 21D, Figure 22A). When the rat's head was inside the ON resonant coil, the device was activated, stimulating dopaminergic neurons in the MFB and inducing a location preference for that coil (Figure 21D, Supplementary Video 4). We quantified this effect by analyzing the amount of time the rat spent in the ON resonant coil compared to the OFF resonant

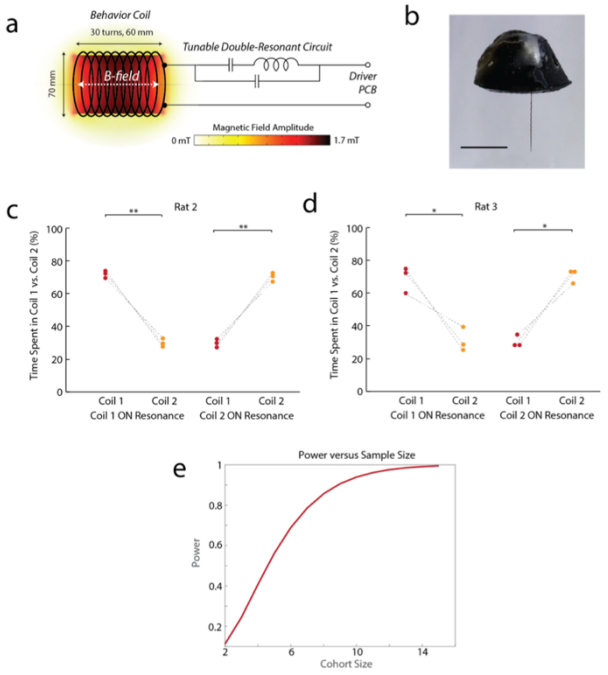

Figure 22 Place Preference Experiment a) Schematic of experimental setup showing the magnetic field circuit and magnetic field strength (b) Image of a fully enclosed ME film implant scale bar = 5 mm (c-d) Individual results of the place preference trials for rats 2 and 3 (e) Suggested power vs sample size for future neuroscience results where power should be >0.8.

coil in six 10-minute trials/rat. To demonstrate that this effect was due to the ME device we performed three trials and then switched which coil was on resonance for another three trials. As expected, we found that the place preference switched to match which coil was on resonance with our implant (Figure 21F,G, Figure 22C,D). In each case we see a significant preference for the ON resonant coil, which confirmed that this fully-implanted biphasic device is an effective neural stimulator. We again performed a power analysis based on this data to determine the approximate cohort size that would be needed for hypothesis testing using this approach (Figure 22E).

4.4.1. Methods

Resonant Coil Design

In order to generate sufficient field strengths of >1mT at the resonant frequencies for the miniature devices (300-400 kHz) we developed a custom resonant coil system as shown in Figure 22. This system had two separate resonant frequencies to be able to selectively active each film on the miniature device. The first higher resonance is determined by a single capacitor C_1 in series with the behavioral coil while the self-resonance from a second inductor acts as a low pass filter to prevent a second capacitor C_2 from affecting the system. The second lower series resonance is determined from adding C_1 and C_2 in parallel as the inductor no longer filters out the lower resonant frequency.

In vivo experiments:

All experiments were approved by the Rice University Institutional Animal Care and Use Committee's guidelines and adhered to the National Institute of Health guidelines. Six adult male Long-Evans rats aged 4-7 months and weighing 500-800 grams from Charles River Laboratories were used for this study. Rats were housed in pairs prior to surgery and randomly chosen for implantation. Post-implantation rats were individually housed. At all times animals were kept on a 12 hour light-dark cycle.

Rat Surgical Procedures

All experiments were approved by the Rice University Institutional Animal Care and Use Committee's guidelines and adhered to the National Institute of Health guidelines. For both rotation tests and place preference animal experiments a total of six male Long-Evans rats (three per experiment weighing in the range of 500-800

grams) were anesthetized with isoflurane gas. Five percent isoflurane was used to induce anesthesia and 1.5-2.5% was used to maintain anesthetic depth. Buprenorphine (0.04mg/kg) was administered prior to ear bars as an analgesic. Following initial setup surgical methods differ for the two experimental protocols. For rotation test experiments, 5-7 skull screws were placed to anchor the electrode array. Skull screws were bound to skull with C&B Metabond (Parkell). A craniotomy was made to accommodate the microelectrode array and expose an injection site for neurotoxin. A 30-gauge needle was bent at the tip to pull away dura covering the brain. Desipramine (DMI) reconstituted in saline at a concentration of 15 mg/mL was injected IP to protect noradrenergic neurons. The dose of DMI was approximately 15 mg/kg and injected approximately 30 minutes prior to administration of neurotoxin. To induce hemiparkinsonian lesion, 8 ug of 6-hydroxydopamine (OHDA) at 2ug/uL in saline was injected at 0.2 uL/min into the medial forebrain bundle (MFB -1.2mm -- -1.25mm ML, -4mm AP and -8.1mm DV). STN stimulation was delivered via 2x2 platinum iridium microelectrode array (Microprobes) with 600 x 600 um spacing of 75 um electrodes. Each electrode had a nominal 10 kOhm impedance. For two rats electrode array was lowered to -2.6mm ML, -3.6mm AP and -8.2mm DV from bregma. For the third rat the electrode array was placed into the brain at 2.5mm ML, -3.4mm AP relative to bregma and -7.7mm DV relative to dura. The array was fixed to the skull with standard two-part dental acrylic. For place preference experiments 3-4 skull screws were placed above bregma. Skull screws were similarly bound to the skull with Metabond dental acrylic; however, the Metabond acrylic was limited to flow only above bregma. A craniotomy and duratomy above the location of the MFB (-1.8mm ML, -2.8mm AP) was made to accomodate for a 9 mm platinum iridium bipolar stereotrode from Microprobes with a nominal 10 kOhm impedance at 1 kHz. A custom 3D printed rounded/smoothened enclosure housing the electronics and connecting to the stimulating electrode was stereotactically lowered into the exposed brain to the depth of the MFB at -8.6mm --8.7mm DV relative to bregma. Kwiksil from World

Precision Instruments was injected into the duratomy site built up to the base of the housing. Metabond was then applied again to the base of the 3D printed housing down to the Metabond on the skull screws. For a final securing of the implant, UVcuring Flow-IT (Pentron) was used to cover the implant and anchor it to the Metabond in order to avoid the heat generated from the curing of standard two-part dental acrylic from damaging the custom housing and electronics. Lastly, the animal skin was sutured over the implant leaving it enclosed underneath the skin. The sutures were found to be strongest and confirmed to hold for at least one month when using minimal (1 -- 2) interrupted sutures over the implant itself.

Hemi-Parkinsonian Experiments

Prior to stimulating each rat with the magnetoelectric stimulator, the stimulator power was estimated via a benchtop approximation of the rodent electrode impedance. Constant current stimulation of the rodent brain with an A-M Systems 4100 stimulator produced characteristic voltage waveforms that approximated a simplified parallel RC circuit. A 56 kOhm resistor, and 440 pF capacitor in parallel closely approximated the impedance characteristics of the rat brain across the stimulating electrodes. Using this circuit model, we estimated the field strengths and pulse durations necessary to produce the desired stimulation effects and confirm that the stimulation was charge balanced prior to rodent experimentation.

Prior to performing the rotation tests the rat was briefly anesthetized with 5% isoflurane gas and injected intraperitoneally (IP) with methamphetamine (0.31 ml 1.25 mg/kg) and the wireless biphasic stimulator was plugged into the implanted electrode array. After the anesthesia had worn off (about 5-10 min) the rat was

placed in the cylindrical behavioral chamber. The magnetic field was applied over the whole behavioral area to the films on the device (Figure 20A).

The magnetic field was applied on resonance and off resonance for one minute at various times during the 40-minute trial. The resonant frequencies were 130 kHz and 160 kHz and the off resonant frequencies were 120 kHz and 170 kHz.

Rodent Tracking

Head position on the rotation task was generated using a slightly modified version of DeepLabCut[108] to track ears, snout, and implant. A dataset totaling 286 frames from both the on and off resonance rotation tasks was hand labeled and trained for approximately 140,000 iterations.

Position during the place preference task was manually tracked via custom python scripts. The overall preference was quantified by counting the number of frames in which the animal was inside either one of the coils.

Place Preference Implant Design

The miniature ME films were fabricated from PZT/Metglas. The circuit components used were the same as those used in the brain slice and rotation test, however in this case there was no circuit board and the elements were soldered together directly and the films attached with conductive epoxy. The films/circuit were parylene coated for extra insulation and then a small bias magnet was attached in the orientation and position that ensured the best charge balance

between the two phases. The plastic case designed to put the least stress on the skin was 3D printed in plastic and included a channel to securely hold the stereotrode and a chamber to hold the circuit/films. The circuit/films were attached to the stereotrode with conductive epoxy and a combination of Flow-It ALC (Pentron) and epoxy were used to encapsulate the entire outside of the box. Prior to implantation the implant was put through a 12 hour ethylene oxide cycle followed by a 12-24 hour degas period inside of a fume hood.

Place Preference Experiments

The rats were given a minimum of 24 hours to recover. We performed the experiments 1-3 days after the surgery. The rat was placed on a linear track with a coil at each end. Both coils applied a resonant alternating magnetic field, but only one was on resonance to activate the implanted device. We took a 10 minute video recording of the rat position starting from the first time the rat received stimulation from the ON resonant coil. After 10 minutes the rat was removed from the track and placed back into the home cage for a minimum of 5 minutes while the track was cleaned. In order to ensure that the rat did not develop associations with specific places in the room, we rotated the track to an arbitrary angle between each of the six trials. In total we performed 6 trials/rat. Between the third and fourth trial the system was also re-tuned to switch which coil was resonant with the device in addition to rotating the track.

Quantification and Statistical Analysis

Error bars in Figure S1m denote +/- one standard deviation for n=~50 data points, n refers to an individual film. We furthermore performed a Tukey's Honest

Significant Difference test on the data in Figure S1m, which indicated that the voltage produced at each different PVDF thickness is significantly different.

Paired t-tests were used for the rodent tests in figures 4 and 5. Star values indicate levels of significance associated with the P-values listed in the figure captions. In figure 4f we compared n=9 data points for before and during off resonance stimulation and n=9 data points for before and during on resonance stimulation where n refers to 1 stimulation period during a trial. In figure 4g we compared n=29 for on resonance data points and n=28 for off resonance data points, where n refers to all the rotation rate data points for all rats during the specified time periods (averages for each rat shown in figure, not individual data points). In figure 5f we compared n=3 data points for each coil during a trial, where n=amount of time spent in one coil compared to the other. In figure 5g we compared n=9 data points (averages for each rat shown in figure, not individual data points) where n=individual data points for amount of time spent in one coil during a trial. The supplemental power analysis was done using MATLAB to estimate a sample size based on potential means and standard deviations of a larger data set from our proof of principle work. Values used in the estimate were as follows: Rotation test: means=11 and 6 rpm, standard deviation=4. Place preference test: means=70 and 30%, standard deviation=20.

Chapter 5

Discussion: Putting ME in context with other form of wireless power transfer

5.1. Advantages, Current Limitations, and Future Prospects

The advantages of ME materials extend beyond these proof-of-principle demonstrations. ME materials have the potential to enable miniature neural stimulators that can be implanted deep in the brain of large animals or humans and activated externally with an electromagnet. Additional miniaturization from the rice-sized device shown here is not expected to reduce the film voltage, suggesting that even smaller films could serve as effective stimulators. In the future, the rectifying diode and/or LED could be fabricated directly onto the ME film using lithography techniques, enabling miniature materials-based ME stimulators.

External ME stimulators such as the one described in the *in vivo* rotation experiment could have an immediate impact on the study of DBS therapies using rodent disease models. Because the ME stimulator is compatible with commercial implanted electrodes, and the magnetic stimulators can be adapted to a number of standard behavioral experiments or animal enclosures, our ME stimulators could readily replace the wired DBS stimulators currently in use. As a result, new experiments can

be developed to probe the effects of chronic and continuous DBS or DBS in social contexts where wired DBS stimulators would be impracticable.

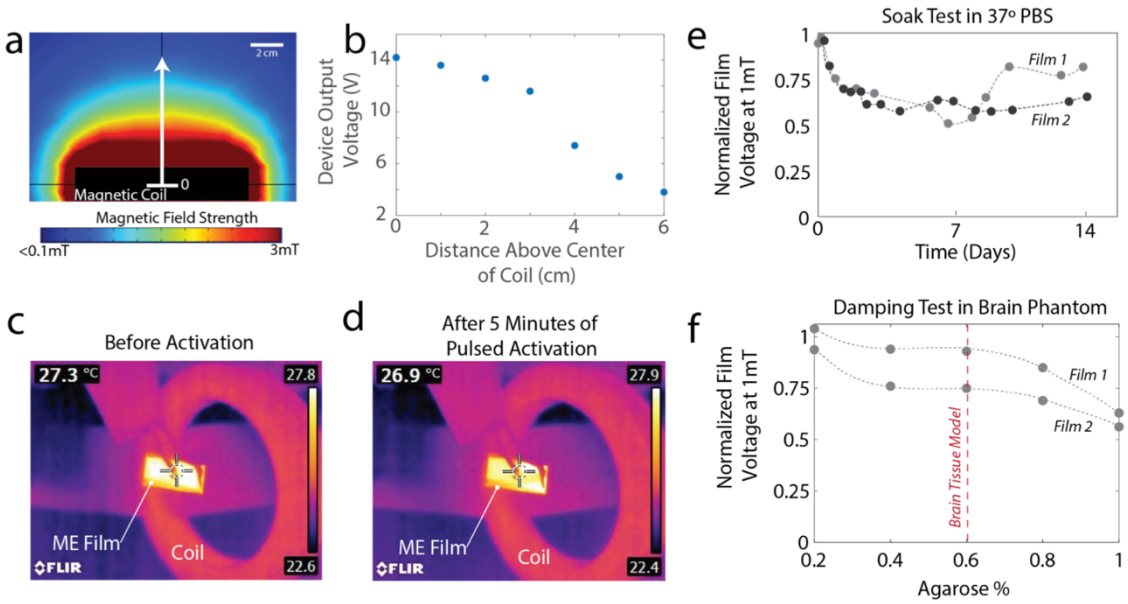

Figure 23 Future Considerations for ME Devices (a) COMSOL simulation of magnetic field above a circular coil and (b) Measured device output voltage as a function of distance above the coil (c-d) Films do not heat up during five minutes of pulsed operation (e) Soak test at 37C shows that film output voltage remains relatively constant for up to 14 days of constant activation (f) Films still show usable voltage even with some damping in agarose brain phantom

Fully implanted ME stimulators have further advantages of avoiding routes for infection and allow for even more freedom of movement and social interaction between animals. Devices like these could also be adapted to target different brain areas or peripheral nerves using commercially available or custom designed electrodes.

Our preliminary lifetime testing showed good performance under physiological conditions, but more work is needed to develop packaging solutions for chronic *in*

vivo applications. Specifically, we found that these miniaturized ME films when encapsulated with polyimide maintained their functionality during a 14-day soak test in 37°C saline (Figure 23E). Additionally, when we placed the coated films into an agarose gel that closely matches the mechanical properties of brain tissue we found only a 20% decrease in voltage as a result of this mechanical dampening (Figure 23F). Because films can produce 10-30 V, we expect these films to function under biological conditions. To avoid dampening, one could design packaging solutions that reduce the mechanical coupling between the film and the tissue. Future testing, including immunohistochemistry, will be needed to assess the foreign body response and develop packaging that limits this response and is stable for chronic use.

For applications that require chronic high frequency stimulation it will be important to measure the internal device losses due to heat and pressure waves and how this could affect tissue. As a preliminary experiment, we measured the temperature of the film following 5 minutes of pulsed activation (ME Film = 6 V_{pp} and 20% duty cycle at 100 Hz) and observed no increase in the film temperature (Figure 23C,D). Should pressure waves pose a hazard, one could develop packaging solutions that minimized the mechanical coupling between the film and the tissue.

The overall volume of the fully implanted stimulator, while small compared to conventional stimulators, remains relatively large compared to other recent implanted technologies (Table 1). However, the size of the ME power source is small (2-4 mm^3 , Table 1) while the bulk of the implant is packaging, bias magnet, and off-the-shelf circuit elements. Further miniaturization is possible with improved layouts and packaging as well as with custom miniature integrated circuits. The realization of all this, together with further deceases in the ME film size could lead to sub-mm sized implantable devices. A potential challenge with future free-floating devices for clinical applications is that they could migrate over time from the target tissue.

Future work should address this and explore methods to anchor or tether the devices using biocompatible adhesives[109], or mechanical anchors like nerve cuffs.[18]

The arena size used in the rotation experiment is comparable to other studies using RF powered devices, and future work should focus on exploring larger arenas and the associated engineering challenges. Our calculations suggest that we can reconfigure the drive coils for a number of behavioral experiments by placing coils beneath the floor of an animal enclosure. Simulations and measurements show that 4-5 cm above a drive coil ME films generate sufficient voltage for some low levels of stimulation (Figure 23A,B). This distance could be further improved by optimizing the geometry of the coils or increasing the power of the magnetic field.

The performance and application space for ME stimulators can be greatly expanded by adding application specific integrated circuits (ASICs). With these circuits one could create biphasic stimulation using a single ME film or generate wirelessly programmable stimulation at various specified voltage levels.[110] Additionally, one can imagine networks of devices that can be individually addressed using wireless network protocols implemented in the ASICs.[45] This ability to ensure safe and effective stimulation with integrated circuits will likely be required for clinical translation of this technology.

We also foresee applications for ME materials as a wireless power technology for more complex implantable bioelectronic devices. For example, the demonstrated ability of ME films to power LEDs implies that ME materials could power implantable optogenetic stimulators, small integrated circuits for physiological monitoring, or transmit data out for closed-loop bioelectronic devices. For wearable technologies, it is also necessary to further miniaturize magnetic field generators so that they can be battery powered and comfortably worn.

With the benefits of ME-based bioelectronics also come limitations. The need for magnetic materials may limit the magnetic imaging compatibility of some devices. Compared to ultrasound and RF wireless power that rely on propagating waves, our ME devices are powered by near-field magnetic fields. As a result, the depth that we can effectively power ME devices depends size of the transmitter. On other hand, the magnetic fields used here show negligible absorption by the tissue allowing us to increase the power in the transmitter and remain well below the safety limits. Together, these considerations provide design tradeoffs when developing a system for miniature bioelectronic implants, where the constraints on the size of the transmitter, need to transmit through air, and total power needed at the device may lead one to choose one wireless power solution over another. Additionally, bidirectional communication based on ME effects may be difficult since the magnetic fields do not radiate like ultrasound or electromagnetic waves.

With this proof of principle work, we can now analyze the tradeoffs and add magnetoelectrics as a sixth form of wireless power transfer to the five discussed in Chapter 2. (Figure 24) While the main in vivo demonstrations of magnetoelectric wireless power transfer for bioelectronic applications use lower frequency magnetic fields (100s of kHz), Nan et al., has shown further miniaturization of ME films to miniature antennas which can be activated by a high frequency RF transmitting antenna. [45,49,111]These two different techniques are similar, yet because the transmitter is different, they have slightly different tradeoffs and application spaces.

For the antenna transmitter version of an ME power system, the main advantage lies in the miniaturization, with feature sizes on the order of hundreds of microns in the GHz range (Figure 24). However, this miniaturization comes with lower power levels compared to other larger acoustic techniques. The depth is again limited by safe levels of RF exposure and because the power levels are already low, the alignment

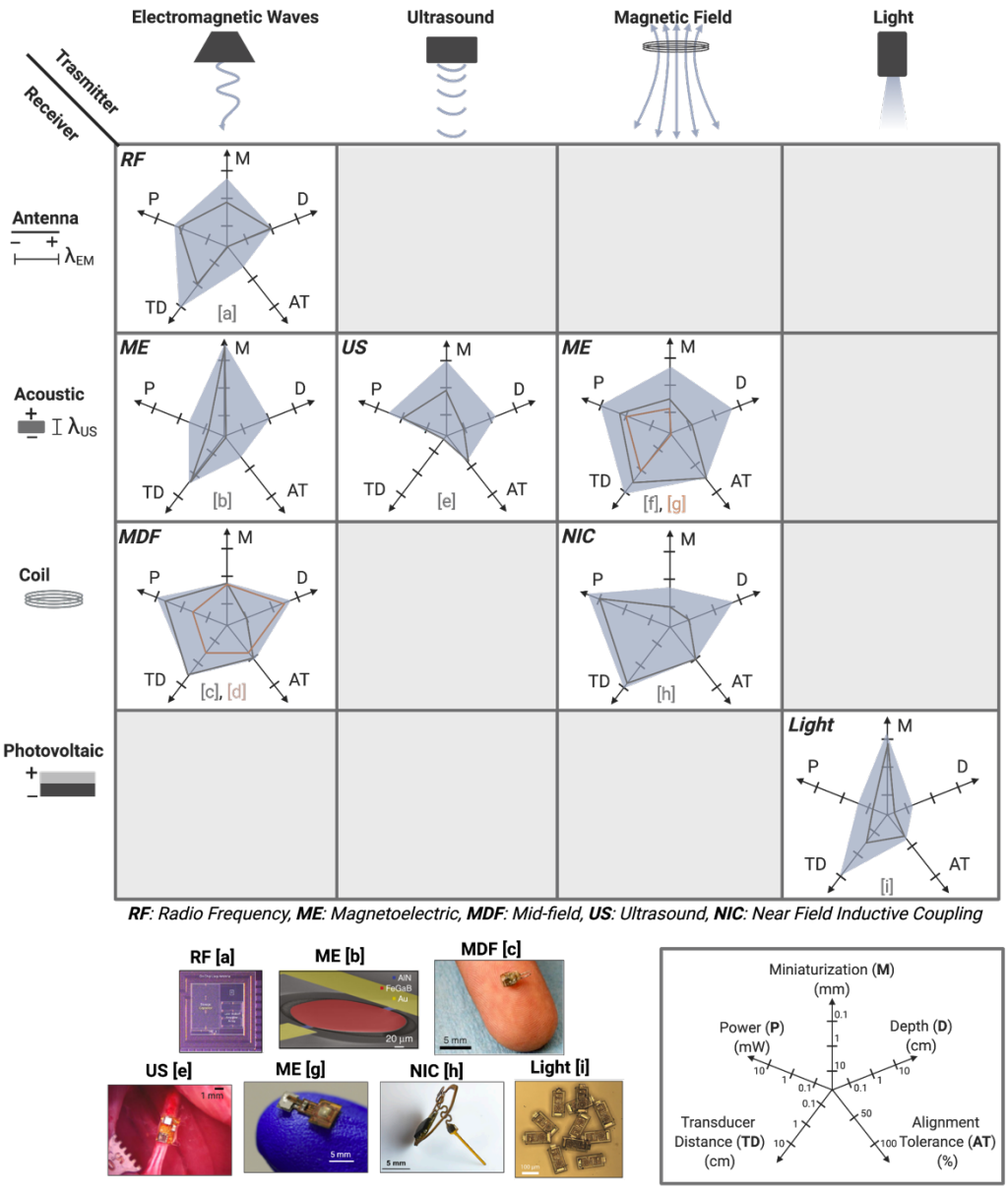

Figure 24 Repeat of Figure 6 with the addition of recent ME technologies

tolerance will likely be reduced compared to systems with higher power levels. Magnetoelectric systems powered by a lower frequency magnetic coil can achieve higher power levels (several mW) with a larger device footprint (feature sizes on the order of several mm). Because magnetic fields at these frequencies can travel

attenuated through air and tissue the depth and transmitter distance can easily approach several cm. These ME devices also have slightly improved alignment tolerance due to the fact that the magnetostrictive layer helps to capture and concentrate the magnetic field along the length of the implant.[45,86] **Overall, magnetoelectrics is an excellent choice to power devices that are mm-sized or smaller particularly if the application requires high-tolerance to translational misalignments or power transfer through air and bone.**

5.2. Further considerations for future bioelectronics

5.2.1. Size and Safety Considerations

While it is challenging to make direct unbiased comparisons across such a diverse array of wireless power technology, we can directly compare the physical size of the devices, the amount of power generated, and, when reported, how close these systems are to the safety limits. In general, there are two different types of safety limits (Figure 25**,** References a[53], b[15], c[32], d[17], e[18], f[30], g[35,41], h[35], i[20]).[28,75,112,113] One

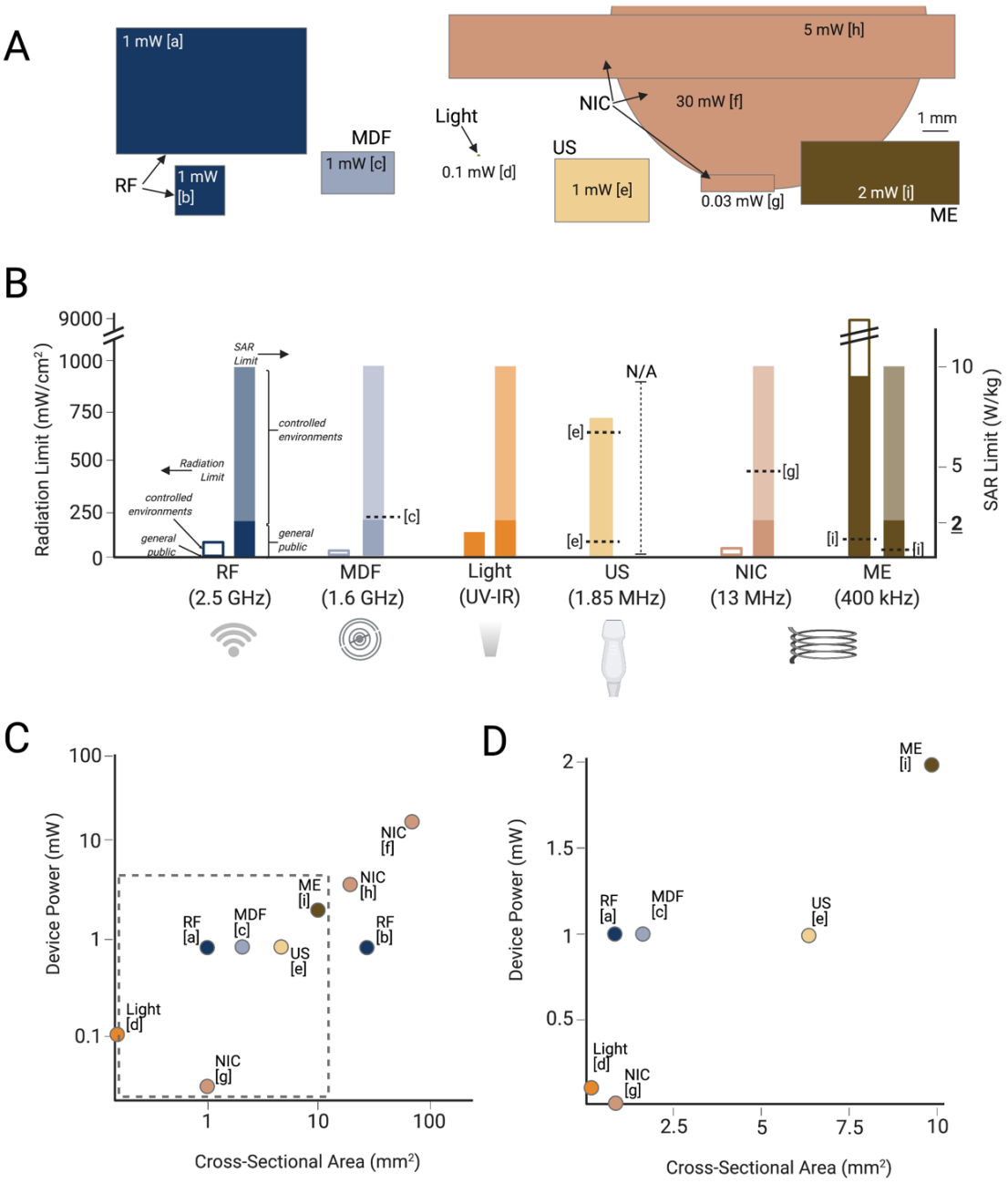

Figure 25 Comparisons of the size, power, and safety limits of miniature devices used in in vivo experiments shows a range of devices sizes and powers (A). The safety limits (B) vary for each type of WPT and, in some cases, devices already operate at or near the limits which limits the transmitter power. Increasing the size of the implant can also increase the generated power (C,D).

based on the levels of radiation tissue can safely handle. The other is specific

absorption rate (SAR) and is based on the rate energy of any type is absorbed by a mass of tissue. Exceeding SAR limits will usually lead to tissue damage from heat. For each transmitter type there are standard safety limits for the general public and for controlled environments. The radiation safety limits are set based on the type of transmitter and the frequency. Figure 25 B shows the general public and controlled environment limits for each type of transmitter discussed above. The SAR limits are the same for all types of transmitters 2 W/kg for the general public and 10 W/kg for controlled environments. When available we also noted the levels used by reported devices in in vivo experiments. In some cases, the devices may also be functional at lower exposure levels and a higher level was used, possibly to ensure in vivo functionality.

There are several conclusions we can draw from these safety limits. As expected, the radiation limits are significantly lower for electromagnetic and higher frequency magnetic forms of power transfer. Furthermore, these low levels combined with the fact that existing technologies in these categories already exceed the general public SAR limits, means that, at least in clinical applications, these types of technologies as described will be limited to controlled environment use like in treatment clinics or preclinical animal use only.

Figure 25A also shows a to-scale comparison of the sizes of various devices described above and the approximate maximum power each device could generate in vivo. Though it is difficult to draw too many quantitative conclusions, in general we can see that the larger devices generate more power (Figure 25C,D). Furthermore, we can see that many methods of wireless power transfer can currently activate implants that are in the1-10 mm^2 size range. Future progress in many of these techniques will push these miniaturization limits to reach new biological targets.

5.2.2. Conclusions and Future Directions

Although there are many metrics one must consider when choosing the right wireless power option for a particular implanted bioelectronic device we attempted here to provide a guide for making this choice and a discussion of the tradeoffs

A

Technology	Advantages	Limitations
RF	*large transmitter-reciever distance*, *easy integration*, *data transfer*	*shallow implants*
MDF	*good all-around performance*	*near safety limits for tissue absorbtion*, *difficult uplink*, *no commercial transmitter*
Light	*smallest implants*	*shallow implants*
US	*very small implants*	*poor alignment tolerance*, *gel or foam contact between skin/transducer*
NIC	*higher power implants*, *easy integration*	*large implants*, *poor alignment tolerance*
ME	*good all-around performance*, *good alignment tolerance*	*difficult uplink*, *no commercial transmitter*, *MRI compatibility*

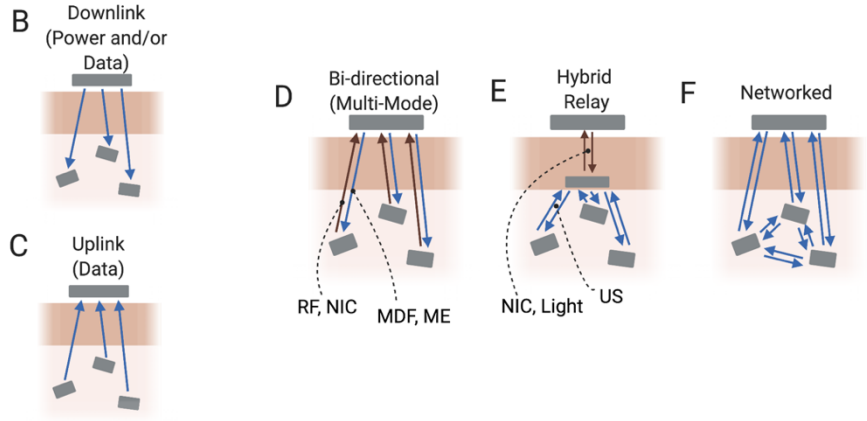

Figure 26 A)Summary of the main advantages and limitations of each WPT method can guide future applications for each modality. Current devices generally use only up to several channels or devices to either stimulate (B) or record (C). Future iterations of bioelectronic devices may combine different modalities to increase channel count and device applications (D-F).

among the six major types of wireless power technologies that have been demonstrated in vivo. Figure 26A summarizes the main advantages and limitations of each of the WPT types discussed here.

Going forward one can consider what types of systems might be possible by using these types of wireless power technologies alone or in combination (Figure 26B-F). Thus far most wireless power transfer techniques have focused on transmission between a single transmitter and a single implanted device in one or more animals to either stimulate or record (Figure 26B,C). In most cases each implant has one stimulation or recording channel, with a few that have two to three channel interfaces for each device. However, many wired or battery powered devices used today use a minimum of four channels for stimulation, and sometimes many more.[114–116] To achieve these higher channel counts it may be necessary to create networks of multiple wireless bioelectronic implants. These networks may one day mix methods for wireless power and data transfer and could form any number of network architectures (Figure 26D-F).[42,45,117,118] These multimode systems can combine the advantages and minimize the limitations of the various WPT techniques. Free from wire and tethers these networks could span large areas of tissue and coordinate multimodal sensory and simulation capabilities to provide precise regulation of physiological processes.[119] Indeed, bioelectronics empowered by a suite of wireless data and power transfer technologies is certain to usher in innovative minimally invasive and distributed systems for improving the way we understand and treat disease.

References

1. Kellaway, P. THE PART PLAYED BY ELECTRIC FISH IN THE EARLY HISTORY OF BIOELECTRICITY AND ELECTROTHERAPY. **20**, (1946).

2. Tiktinsky, R., Chen, L. & Narayan, P. Electrotherapy: yesterday, today and tomorrow. **16**, 126–131 (2010).

3. Volkow, N. D., Collins, F. S. & Ph, D. The Role of Science in Addressing the Opioid Crisis. 391–394 (2017).

4. Cogan, S. F. Neural stimulation and recording electrodes. *Annual Review of Biomedical Engineering* **10**, 275–309 (2008).

5. Zhao, Z. *et al.* Parallel, minimally-invasive implantation of ultra-flexible neural electrode arrays. *Journal of Neural Engineering* **16**, (2019).

6. Fan, B., Rodriguez, A. v, Vercosa, D. G., Kemere, C. & Robinson, J. T. Sputtered porous Pt for wafer-scale manufacture of low-impedance flexible microelectrodes. *Journal of Neural Engineering* **17**, (2020).

7. Mekhail, N. A. *et al.* Retrospective Review of 707 Cases of Spinal Cord Stimulation: Indications and Complications. *Pain Practice* **11**, 148–153 (2011).

8. Deer, T. R. & Stewart, C. D. Complications of spinal cord stimulation: Identification, treatment, and prevention. *Pain Medicine* **9**, (2008).

9. Biran, R., Martin, D. C. & Tresco, P. A. The brain tissue response to implanted silicon microelectrode arrays is increased when the device is tethered to the skull. *Journal of biomedical materials research. Part A* **82**, 169–178 (2007).

10. Bock, D. C., Marschilok, A. C., Takeuchi, K. J. & Takeuchi, E. S. Batteries used to power implantable biomedical devices. *Electrochimica Acta* **84**, 155–164 (2012).

11. Schmidt, C. L. & Skarstad, P. M. The future of lithium and lithium-ion batteries in implantable medical devices. *Journal of Power Sources* **97–98**, 742–746 (2001).

12. Balcombe, J. P., Barnard, N. D. & Sandusky, C. Laboratory routines cause animal stress. *Journal of the American Association for Laboratory Animal Science* **43**, 42–51 (2004).

13. Yu, Z. *et al.* An 8.2mm 3 Implantable Neurostimulator with Magnetoelectric Power and Data Transfer. in *International Solid-State Circuits Conference* vol. 58 6–8 (2020).

14. Burton, A. *et al.* Wireless, battery-free subdermally implantable photometry systems for chronic recording of neural dynamics. *Proceedings of the National Academy of Sciences of the United States of America* **117**, 2835–2845 (2020).

15. Rahmani, H. & Babakhani, A. A wireless power receiver with an on-chip antenna for millimeter-size biomedical implants in 180 nm SOI CMOS. *IEEE MTT-S International Microwave Symposium Digest* 300–303 (2017) doi:10.1109/MWSYM.2017.8059103.

16. Ho, J. S. *et al.* Wireless power transfer to deep-tissue microimplants. *Proceedings of the National Academy of Sciences of the United States of America* **111**, 7974–7979 (2014).

17. Cortese, A. J. *et al.* Microscopic sensors using optical wireless integrated circuits. *Proceedings of the National Academy of Sciences* **117**, 9173–9179 (2020).

18. Piech, D. K. *et al.* A wireless millimetre-scale implantable neural stimulator with ultrasonically powered bidirectional communication. *Nature Biomedical Engineering* **4**, 207–222 (2020).

19. Olds, J. & Milner, P. Positive reinforcement produced by electrical stimulation of septal area and other regions of rat brain. *Journal of comparative and physiological psychology* **47**, 419–427 (1954).

20. Singer, A. *et al.* Magnetoelectric Materials for Miniature , Wireless Neural Stimulation at Therapeutic Frequencies. *Neuron* (2020).

21. Piech, D. K. *et al.* A wireless millimetre-scale implantable neural stimulator with ultrasonically powered bidirectional communication. *Nature Biomedical Engineering* **4**, 207–222 (2020).

22. Caruana, F., Jezzini, A., Sbriscia-Fioretti, B., Rizzolatti, G. & Gallese, V. Emotional and social behaviors elicited by electrical stimulation of the insula in the macaque monkey. *Current Biology* **21**, 195–199 (2011).

23. Lockard, J. S., Congdon, W. C. & DuCharme, L. L. Feasibility and safety of vagal stimulation in monkey model. *Epilepsia* **31 Suppl 2**, S20-6 (1990).

24. Lozano, A. M., Dostrovsky, J., Chen, R. & Ashby, P. Deep brain stimulation for Parkinson's disease: Disrupting the disruption. *Lancet Neurology* **1**, 225–231 (2002).

25. Clark, K. B., Naritoku, D. K., Smith, D. C., Browning, R. A. & Jensen, R. A. Enhanced recognition memory following vagus nerve stimulation in human subjects. *Nature Neuroscience* **2**, 94–98 (1999).

26. Jennifer Morton, A. & Howland, D. S. Large genetic animal models of huntington's disease. *Journal of Huntington's Disease* **2**, 3–19 (2013).

27. Chung, B. S. *et al.* Rise of the Visible Monkey: Sectioned images of rhesus monkey. *Journal of Korean Medical Science* **34**, 1–15 (2019).

28. *IEEE Standard for Safety Levels with Respect to Human Exposure to Radio Frequency Electromagnetic Fields , 3 kHz to 300 GHz*. vol. 2005 (2006).

29. Maeng, L. Y. *et al.* Behavioral validation of a wireless low-power neurostimulation technology in a conditioned place preference task. *Journal of Neural Engineering* **16**, 026022 (2019).

30. Shin, G. *et al.* Flexible Near-Field Wireless Optoelectronics as Subdermal Implants for Broad Applications in Optogenetics. *Neuron* **93**, 509-521.e3 (2017).

31. Montgomery, K. L. *et al.* Wirelessly powered, fully internal optogenetics for brain, spinal and peripheral circuits in mice. *Nature Methods* **12**, 969–974 (2015).

32. Agrawal, D. R. *et al.* Conformal phased surfaces for wireless powering of bioelectronic microdevices. *Nature Biomedical Engineering* **1**, 1–16 (2017).

33. Rampengan, S. H., Wijaya, H., Yoga, G., Pangemanan, J. A. & Panda, A. L. Leadless permanent pacemaker : an article review. **48**, 5–12 (2017).

34. Mulpuru, S., Madhavan, M., McLeod, C., Cha, Y.-M. & Friedman, P. Cardiac Pacemakers : Function , Troubleshooting , and Management. *Journal of the American College of Cardiology* **69**, 189–210 (2017).

35. Loeb, G. E., Peck, R. A., Moore, W. H. & Hood, K. BION™ system for distributed neural prosthetic interfaces. *Medical Engineering and Physics* **23**, 9–18 (2001).

36. Suarez-Cedeno, G., Suescun, J. & Schiess, M. C. Earlier Intervention with Deep Brain Stimulation for Parkinson's Disease. *Parkinson's Disease* **2017**, (2017).

37. Chaffee, E. L. & Light, R. U. A Method for the Remote Control of Electrical Stimulation of the Nervous System. *The Yale Journal of Biology and Medicine* **7**, 83–128 (1934).

38. Bear, Z. W. & Mikulec, A. A. Turn on the Music: Cochlear Implants. *Missouri medicine* **113**, 68–71 (2016).

39. Shiramatsu, T. I. *et al.* Effect of vagus nerve stimulation on neural adaptation in thalamo-cortical system in rats. *Proceedings of the Annual International Conference of the IEEE Engineering in Medicine and Biology Society, EMBS* **2016-Octob**, 1834–1837 (2016).

40. Talwar, S. K. *et al.* Rat navigation guided by remote control. *Nature* **417**, 37–38 (2002).

41. Freeman, D. K. *et al.* A sub-millimeter, inductively powered neural stimulator. *Frontiers in Neuroscience* **11**, 1–12 (2017).

42. Lyu, H. *et al.* Synchronized Biventricular Heart Pacing in a Closed-chest Porcine Model based on Wirelessly Powered Leadless Pacemakers. *Scientific Reports* **10**, 1–9 (2020).

43. Barbruni, G. L., Ros, P. M., Demarchi, D., Carrara, S. & Ghezzi, D. Miniaturised Wireless Power Transfer Systems for Neurostimulation: A Review. *IEEE Transactions on Biomedical Circuits and Systems* **14**, 1160–1178 (2020).

44. Chen, R., Canales, A. & Anikeeva, P. Neural recording and modulation technologies. *Nature Reviews Materials* **2**, 1–16 (2017).

45. Yu, Z. *et al.* MagNI: A Magnetoelectrically Powered and Controlled Wireless Neurostimulating Implant. *IEEE Transactions on Biomedical Circuits and Systems* **14**, 1241–1252 (2020).

46. Fotopoulou, K. & Flynn, B. W. Wireless Power Transfer in Loosely Coupled Links : Coil Misalignment Model. *IEEE Transactions on Magnetics* **47**, 416–430 (2011).

47. Aldaoud, A. *et al.* Wide dipole antennas for wireless powering of miniaturised bioelectronic devices. *Sensing and Bio-Sensing Research* **27**, 100311 (2020).

48. Karnaushenko, D. D., Karnaushenko, D., Makarov, D. & Schmidt, O. G. Compact helical antenna for smart implant applications. *NPG Asia Materials* **7**, 1–10 (2015).

49. Nan, T. *et al.* Acoustically actuated ultra-compact NEMS magnetoelectric antennas. *Nature Communications* **8**, 1–7 (2017).

50. Yazdandoost, K. Y. A 2.4 GHz antenna for medical implanted communications. *APMC 2009 - Asia Pacific Microwave Conference 2009* 1775–1778 (2009) doi:10.1109/APMC.2009.5384240.

51. Sun, Y. *et al.* Wirelessly Powered Implantable Pacemaker with On - Chip Antenna. *IEEE* 1242–1244 (2017).

52. Liu, C., Guo, Y. X., Sun, H. & Xiao, S. Design and safety considerations of an implantable rectenna for far-field wireless power transfer. *IEEE Transactions on Antennas and Propagation* **62**, 5798–5806 (2014).

53. Park, S. il *et al.* Stretchable multichannel antennas in soft wireless optoelectronic implants for optogenetics. *Proceedings of the National Academy of Sciences* **113**, E8169–E8177 (2016).

54. Chi, A. *et al.* A 1 V 5 mA Multimode IEEE 802.15.6/Bluetooth Low-Energy WBAN Transceiver for Biotelemetry Applications. **48**, 186–198 (2013).

55. Tokuda, T. *et al.* 1 mm3-sized optical neural stimulator based on CMOS integrated photovoltaic power receiver. *AIP Advances* **8**, (2018).

56. Bandodkar, A. J. *et al.* Soft, stretchable, high power density electronic skin-based biofuel cells for scavenging energy from human sweat. *Energy and Environmental Science* **10**, 1581–1589 (2017).

57. Leung, V. W. *et al.* A CMOS Distributed Sensor System for High-Density Wireless Neural Implants for Brain-Machine Interfaces. *ESSCIRC 2018 - IEEE 44th European Solid State Circuits Conference* 271–273 (2018) doi:10.1109/ESSCIRC.2018.8494335.

58. Chen, X., Yeoh, W. G., Choi, Y. B., Li, H. & Singh, R. A 2.45-GHz near-field RFID system with passive on-chip antenna tags. *IEEE Transactions on Microwave Theory and Techniques* **56**, 1397–1404 (2008).

59. Ho, J. S. *et al.* Self-Tracking Energy Transfer for Neural Stimulation in Untethered Mice. *Physical Review Applied* **024001**, 1–6 (2015).

60. Ma, A. & Poon, A. S. Y. Midfield wireless power transfer for bioelectronics. *IEEE Circuits and Systems Magazine* **15**, 54–60 (2015).

61. Tajima, K. *et al.* Wireless optogenetics protects against obesity via stimulation of non-canonical fat thermogenesis. *Nature Communications* **11**, 1–5 (2020).

62. Tanabe, Y. *et al.* High-performance wireless powering for peripheral nerve neuromodulation systems. *PLoS ONE* **12**, 1–13 (2017).

63. Carrara, N. Dielectric Properties of Body Tissues in the frequency range 10 Hz - 100 GHz. http://niremf.ifac.cnr.it/tissprop/#refs.

64. Seo, D. *et al.* Wireless Recording in the Peripheral Nervous System with Ultrasonic Neural Dust. *Neuron* **91**, 529–539 (2016).

65. Wu, X. *et al.* Sono-optogenetics facilitated by a circulationdelivered rechargeable light source for minimally invasive optogenetics. *Proceedings of the National Academy of Sciences of the United States of America* **116**, 26332–26342 (2019).

66. Alam, M. *et al.* Development of a battery-free ultrasonically powered functional electrical stimulator for movement restoration after paralyzing spinal cord injury. *Journal of NeuroEngineering and Rehabilitation* **16**, 1–14 (2019).

67. Phillips, W. B., Towe, B. C. & Larson, P. J. An Ultrasonically-Driven Piezoelectric Neural Stimulator. *Annual International Conference of the IEEE Engineering in Medicine and Biology - Proceedings* **2**, 1983–1986 (2003).

68. Oelze, M. L., Miller, R. J., Blue, J. P., Zachary, J. F. & O'Brien, W. D. Estimation of the acoustic impedance of lung versus level of inflation for different species and ages of animals. *The Journal of the Acoustical Society of America* **124**, 2340–2352 (2008).

69. O'Brien, W. D. *et al.* Ultrasound-induced lung hemorrhage: Role of acoustic boundary conditions at the pleural surface. *The Journal of the Acoustical Society of America* **111**, 1102–1109 (2002).

70. Clement, G. T. & Hynynen, K. Physics in Medicine & Biology Related content A non-invasive method for focusing ultrasound through the human skull A non-invasive method for focusing ultrasound through the human skull. *Physics in Medicine and Biology* **47**, 1219 (2002).

71. Hynynen, K., McDannold, N., Sheikov, N. A., Jolesz, F. A. & Vykhodtseva, N. Local and reversible blood-brain barrier disruption by noninvasive focused ultrasound at frequencies suitable for trans-skull sonications. *NeuroImage* **24**, 12–20 (2005).

72. Yang, Z. & Zu, J. Comparison of PZN-PT, PMN-PT single crystals and PZT ceramic for vibration energy harvesting. *Energy Conversion and Management* **122**, 321–329 (2016).

73. Wan, C. & Bowen, C. R. Multiscale-structuring of polyvinylidene fluoride for energy harvesting: the impact of molecular-, micro- and macro-structure. *J. Mater. Chem. A* **5**, 3091–3128 (2017).

74. Tressler, J. F., Alkoy, S. & Newnham, R. E. Piezoelectric Sensors and Sensor Materials. *Journal of Electroceramics* **2**, 257–272 (1998).

75. FDA. Marketing Clearance of Diagnostic Ultrasound Systems and Transducers- Guidance for Industry and Food and Drug Administration Staff. *U.S. Department of Health and Human Services: Food and Drug Administration: Center for Devices and Radiological Health* 18–34 (2019).

76. Zhao, J. *et al.* Self-Powered Implantable Medical Devices: Photovoltaic Energy Harvesting Review. *Advanced Healthcare Materials* **9**, 1–22 (2020).

77. Wang, L. *et al.* Photovoltaic retinal prosthesis: Implant fabrication and performance. *Journal of Neural Engineering* **9**, (2012).

78. Jegadeesan, R., Agarwal, K., Guo, Y. X., Yen, S. C. & Thakor, N. v. Wireless Power Delivery to Flexible Subcutaneous Implants Using Capacitive Coupling. *IEEE Transactions on Microwave Theory and Techniques* **65**, 280–292 (2017).

79. Dagdeviren, C. *et al.* Conformal piezoelectric energy harvesting and storage from motions of the heart, lung, and diaphragm. *Proceedings of the National Academy of Sciences of the United States of America* **111**, 1927–1932 (2014).

80. Ouyang, H. *et al.* Symbiotic cardiac pacemaker. *Nature Communications* **10**, 1–10 (2019).

81. Han, M. *et al.* Three-dimensional piezoelectric polymer microsystems for vibrational energy harvesting, robotic interfaces and biomedical implants. *Nature Electronics* **2**, 26–35 (2019).

82. Zheng, Q. *et al.* Biodegradable triboelectric nanogenerator as a life-time designed implantable power source. *Science Advances* **2**, 1–10 (2016).

83. Dong, C. *et al.* High-efficiency super-elastic liquid metal based triboelectric fibers and textiles. *Nature Communications* **11**, 1–9 (2020).

84. Fetisov, L. Y. *et al.* Nonlinear converse magnetoelectric effects in a ferromagnetic-piezoelectric bilayer. *Applied Physics Letters* **113**, (2018).

85. Zhai, J., Dong, S., Xing, Z., Li, J. & Viehland, D. Giant magnetoelectric effect in Metglas/polyvinylidene-fluoride laminates. *Applied Physics Letters* **89**, 87–90 (2006).

86. Fang, Z., Lu, S., Mokhariwale, N., el Tachchi, M. & Zhang, Q. A New Method to Increase the Magnetoelectric Voltage Coefficients of Metglas/PVDF Laminate Composites. *Mater. Res. Soc. Symp. Proc.* **1199**, (2010).

87. Chen, Z., Su, Y. & Meguid, S. A. The effect of field-orientation on the magnetoelectric coupling in Terfenol-D/PZT/Terfenol-D laminated structure. *Journal of Applied Physics* **116**, (2014).

88. Li, M., Wang, Z., Wang, Y., Li, J. & Viehland, D. Giant magnetoelectric effect in self-biased laminates under zero magnetic field. *Applied Physics Letters* **102**, 8–11 (2013).

89. Kulkarni, a. *et al.* Giant magnetoelectric effect at low frequencies in polymer-based thin film composites. *Applied Physics Letters* **104**, 0–5 (2014).

90. Schabrun, S. M., Jones, E., Elgueta Cancino, E. L. & Hodges, P. W. Targeting chronic recurrent low back pain from the top-down and the bottom-up: a combined transcranial direct current stimulation and peripheral electrical stimulation intervention. *Brain Stimul* **7**, 451–459 (2014).

91. Kesar, T. M. *et al.* Novel Patterns of Functional Electrical Stimulation Have an Immediate Effect on Dorsiflexor Muscle Function During Gait for People Poststroke. *Physical Therapy* **90**, 55–66 (2010).

92. Baizabal-Carvallo, J. F. & Alonso-Juarez, M. Low-frequency deep brain stimulation for movement disorders. *Parkinsonism and Related Disorders* **31**, 14–22 (2016).

93. Theodore, W. H. & Fisher, R. S. Review Brain stimulation for epilepsy. *The Lancet* **3**, 111–118 (2004).

94. Alonso, P. *et al.* Deep brain stimulation for obsessive-compulsive disorder: A meta-analysis of treatment outcome and predictors of response. *PLoS ONE* **10**, 1–16 (2015).

95. de Hemptinne, C. *et al.* Therapeutic deep brain stimulation reduces cortical phase-amplitude coupling in Parkinson's disease. *Nature Neuroscience* **18**, 779–786 (2015).

96. Bewernick, B. H. *et al.* Nucleus Accumbens Deep Brain Stimulation Decreases Ratings of Depression and Anxiety in Treatment-Resistant Depression. *Biological Psychiatry* **67**, 110–116 (2010).

97. Amar, A. ben, Kouki, A. B. & Cao, H. Power approaches for implantable medical devices. *Sensors (Switzerland)* **15**, 28889–28914 (2015).

98. Park, J. *et al.* Screening fluorescent voltage indicators with spontaneously spiking HEK cells. *PLoS ONE* **8**, 1–10 (2013).

99. Jin, L. *et al.* Single Action Potentials and Subthreshold Electrical Events Imaged in Neurons with a Fluorescent Protein Voltage Probe. *Neuron* **75**, 779–785 (2012).

100. Grossman, N. *et al.* Noninvasive Deep Brain Stimulation via Temporally Interfering Electric Fields. *Cell* **169**, 1029-1041.e16 (2017).

101. So, R. Q., Mcconnell, G. C. & Grill, W. M. Frequency-dependent , transient effects of subthalamic nucleus deep brain stimulation on methamphetamine-induced circling and neuronal activity in the hemiparkinsonian rat. *Behavioural Brain Research* **320**, 119–127 (2017).

102. Bottomley, P. A. & Andrew, E. R. RF magnetic field penetration, phase shift and power dissipation in biological tissue: Implications for NMR imaging. *Physics in Medicine and Biology* **23**, 630–643 (1978).

103. Merrill, D. R., Bikson, M. & Jefferys, J. G. R. Electrical stimulation of excitable tissue: Design of efficacious and safe protocols. *Journal of Neuroscience Methods* **141**, 171–198 (2005).

104. Keller, D., Erö, C. & Markram, H. Cell Densities in the Mouse Brain : A Systematic Review. *Frontiers in Neuroanatomy* **12**, (2018).

105. Agmon, A. & Connors, B. W. Thalamocortical responses of mouse somatosensory (barrel) cortexin vitro. *Neuroscience* **41**, 365–379 (1991).

106. Ting, J. T., Daigle, T. L., Chen, Q. & Feng, G. Acute brain slice methods for adult and aging animals: application of targeted patch clampanalysis and optogenetics. *Methods in molecular biology (Clifton, N.J.)* **1183**, 221–242 (2014).

107. Summerson, S. R., Aazhang, B. & Kemere, C. T. Characterizing Motor and Cognitive Effects Associated With Deep Brain Stimulation in the GPi of Hemi-Parkinsonian Rats. *IEEE Transactions on Neural Systems and Rehabilitation Engineering* **22**, 1218–1227 (2014).

108. Mathis, A. *et al.* DeepLabCut: markerless pose estimation of user-defined body parts with deep learning. *Nature Neuroscience* **21**, (2018).

109. Mahdavi, A. *et al.* A biodegradable and biocompatible gecko-inspired tissue adhesive. *Proceedings of the National Academy of Sciences of the United States of America* **105**, 2307–2312 (2008).

110. Yu, Z. *et al.* An 8.2mm 3 Implantable Neurostimulator with Magnetoelectric Power and Data Transfer. in *International Solid-State Circuits Conference* vol. 58 6–8 (2020).

111. Singer, A. *et al.* Magnetoelectric Materials for Miniature , Wireless Neural Stimulation at Therapeutic Frequencies. *Neuron* (2020).

112. Duck, F. A. Medical and non-medical protection standards for ultrasound and infrasound. *Progress in Biophysics and Molecular Biology* **93**, 176–191 (2007).

113. *Human Exposure to Radiofrequency Electromagnetic Fields*. vol. 85 https://www.govinfo.gov/content/pkg/FR-2020-04-06/pdf/2020-06966.pdf (2020).

114. Medtronic. PERCEPT™ PC NEUROSTIMULATOR WITH BRAINSENSE™ TECHNOLOGY FOR DBS THERAPY. https://www.medtronic.com/content/dam/medtronic-com/products/neurological/dbs/documents/dbs-percept-pc-hcp-brochure.pdf.

115. North, R. B., Ewend, M. G., Lawton, M. T. & Piantadosi, S. Spinal cord stimulation for chronic, intractable pain: Superiority of "multi-channel" devices. *Pain* **44**, 119–130 (1991).

116. Verrills, P., Sinclair, C. & Barnard, A. A review of spinal cord stimulation systems for chronic pain. *Journal of Pain Research* **9**, 481–492 (2016).

117. Seo, D., Carmena, J. M., Rabaey, J. M., Maharbiz, M. M. & Alon, E. Model validation of untethered, ultrasonic neural dust motes for cortical recording. *Journal of Neuroscience Methods* **244**, 114–122 (2015).

118. Khalifa, A. *et al.* The Microbead: A Highly Miniaturized Wirelessly Powered Implantable Neural Stimulating System. *IEEE Transactions on Biomedical Circuits and Systems* **12**, 521–531 (2018).

119. Bhave, G., Chen, J. C., Singer, A., Sharma, A. & Robinson, J. T. Distributed sensor and actuator networks for closed-loop bioelectronic medicine. *Materials Today* (2021) doi:10.1016/j.mattod.2020.12.020.

Appendix A

Table 1. Comparison of Miniature Neural Stimulators

Technology	Inductive Optogenetics	E-Particle	Mid-Field	Mid-Field	Stim Dust	RF Antenna	Magneto Thermal 1	Magneto Thermal 2	This Work Demo 1	This Work Demo 2
Reference[a]	[a]	[b]	[c]	[d]	[e]	[f]	[g]	[h]	This work	This work
Power type (implant)	Inductive coil	Inductive coil	Mid-field coil	Mid-field coil	Piezo electric	RF antenna	Nano-particle injection	Nano-particle injection	Magneto electric	Magneto electric
Activation by:	Magnetic field	Magnetic field	Electro magnetic	Electro magnetic	Ultra-sound	Electro magnetic	Magnetic field	Magnetic field	Magnetic field	Magnetic field
Carrier frequency	13.56 MHz	10.9 MHz	1.5 GHz	1.6 GHz	1.85 MHz	2.3-3.2 GHz	500 kHz	500 kHz	100–170 kHz	250–400 kHz
Stimulation type	LED	Electrical	LED	Electrical	Electrical	LED	Heat	Heat	Electrical	Electrical
Whole implant size (mm^3)	100	0.5	10–25	15	6.5	24	N/A	N/A	500	175
Size of power source (mm^3)	40	0.25	5	5	~0.5	20	N/A	N/A	20	2–4
Implant weight (mg)	30		25–50	70	10	33			500	500
Max implant power (in animal, mW)	30	0.036[b]	10	2	0.35		N/A	N/A	0.1–0.2	2
Demonstrated charge balance (y/n)	N/A	No	N/A	No	Yes	N/A	N/A	N/A	Yes	Yes
Freely moving (y/n)	Yes	Yes	Yes	No	No	Yes	No	Yes	Yes	Yes
Arena volume (cm^3)	12,000	1,000[b]	1,000	N/A	N/A	Video tracked area	N/A	300	3,000–7,000	500
Magnetic field strength (mT)		0.04					19	9.4	1–2	1–2
Genetic modification (y/n)	Yes	No	Yes	No	No	Yes	Yes	Yes	No	No
Fully implanted (y/n)	Yes	Yes	Yes	Yes	Yes	Yes	Yes	Yes	No	Yes
Stimulation frequency (Hz)		50		~3	2 Khz		<1 (0.02)	<1 (0.005)	200	150
Required power (W)			4					7500	30	7

N/A, not applicable

[b]Estimated based on published data

[a]References: [a], Shin et al. (2017); [b], Freeman et al. (2017), Maeng et al. (2019); [c], Montgomery et al. (2015); [d], Ho et al. (2015); [e], Piech et al. (2020); [f], Park et al. (2016); [g], Chen et al. (2015); [h], Munshi et al. (2017)

Table 1